Diopside, enstatite and forsterite solubilities in H_2O and H_2O-NaCl solutions at lower crustal and upper mantle conditions

Catherine A. Macris [a,b,*], Robert C. Newton [a], Jeremy Wykes [c], Ruiguang Pan [b], Craig E. Manning [a]

[a] *Department of Earth, Planetary, and Space Sciences, University of California at Los Angeles, Los Angeles, CA 90095-1567, USA*
[b] *Department of Earth Sciences, Indiana University – Purdue University Indianapolis, IN 46202, USA*
[c] *ANSTO Australian Synchrotron, 800 Blackburn Road, Clayton, VIC 3168, Australia*

Abstract

The interaction of fluids with rock-forming minerals plays an important role in the chemical evolution of mafic and ultramafic rocks in the lower crust and upper mantle. Recent work highlights the importance of salt-rich fluids in element transport in settings such as the mantle wedge above subduction zones and high-grade granulite facies metamorphism. Forsterite (Mg_2SiO_4), enstatite ($MgSiO_3$) and diopside ($CaMgSi_2O_6$) are key rock-forming minerals in these settings in the system CaO-MgO-SiO_2. We determined experimentally the solubilities of diopside, enstatite and forsterite in H_2O-NaCl fluids at a range of pressures and temperatures. Forsterite solubility was determined at 1 GPa, 800 and 900 °C, in pure H_2O and in H_2O-NaCl solutions. Forsterite dissolved congruently at nearly all conditions. Its solubility in pure H_2O is low, but increases greatly with rising NaCl concentration in the fluid. Enstatite solubility was investigated in H_2O-NaCl solutions at 1 GPa, 800 and 900 °C. Enstatite dissolved incongruently to yield forsterite at all conditions. Addition of excess silica led to suppression of forsterite and showed that fluids in equilibrium with enstatite with or without forsterite are strongly enriched in Si relative to Mg, though Mg solubility is significant at high salinity. Diopside solubility was determined in pure H_2O at 650–900 °C and 0.7–1.5 GPa, and in H_2O-NaCl solutions at 800 °C and 1 GPa, with NaCl concentrations approaching halite saturation. Diopside dissolves incongruently yielding residual forsterite at all conditions investigated. The solubility of diopside in pure H_2O increases with increasing pressure, temperature and salinity. Diopside dissolution in H_2O-NaCl solutions displays a dependence on fluid salinity similar to that of forsterite and wollastonite. The results of forsterite solubility experiments in H_2O-NaCl solutions were used to calculate the compositions of fluid coexisting with enstatite or diopside where forsterite was present. The concentration of solutes coexisting with enstatite decreases with rising NaCl, similar to quartz. In contrast, bulk solutes coexisting with diopside increase with NaCl, similar to wollastonite and forsterite. These patterns imply complexing among rock-forming components and fluid components, that Ca-chloride species are substantially more stable than Mg-chloride species, and that hydrous Na-silicate complexes are important components of deep H_2O-NaCl fluids. The results show that salt-bearing brines have substantial metasomatic power and may exert significant control on the chemical evolution of lower crustal and upper mantle mafic and ultramafic rocks.
© 2020 Elsevier Ltd. All rights reserved.

Keywords: Metamorphic fluids; Mineral solubility; Experimental petrology; Mantle metasomatism; Fluid-rock interaction

* Corresponding author at: Department of Earth Sciences, Indiana University - Purdue University Indianapolis, IN 46202, USA.
E-mail address: camacris@iupui.edu (C.A. Macris).

1. INTRODUCTION

The release of aqueous fluids by devolatilization of hydrous minerals and magmas drives mass transfer in a wide range of high-pressure geologic settings. These deep fluids differ fundamentally from shallow and surficial fluids. Shallow fluids range from water rich to saline brines whose maximum salinity is limited by relatively low concentrations at salt-mineral saturation, and the total concentrations of other dissolved solutes are comparatively low (Yardley and Graham, 2002; Yardley and Bodnar, 2014). In contrast, deep fluids are chiefly comprised of H_2O, CO_2, halogen salts (mainly metal chlorides) and dissolved rock components, and may be present as a single phase or an immiscible mixture of CO_2-rich vapor and salt-rich brine (e.g., Manning, 2018). The presence of CO_2 tends to reduce silicate mineral solubility in aqueous fluids and thus lower the capacity for metasomatic mass transfer (e.g., Newton and Manning, 2000a, 2009, 2010). However, halogen salts can dramatically increase solubility and are increasingly recognized as important components of fluids in the lower crust and upper mantle (Newton et al., 1998; Newton and Manning, 2010; Manning and Aranovich, 2014).

The most abundant halogen in terrestrial fluids is chlorine. Chloride-rich solutions play an important role in metasomatic mass transfer in subduction-zones (Scambelluri and Philippot, 2001; Keppler, 2017; Barnes et al., 2018). Evidence includes fluid inclusions in slab lithologies (e.g., Philippot and Selverstone, 1991) and in the mantle wedge (e.g., Kawamoto et al., 2013), melt inclusions in arc volcanics (e.g., Wallace, 2005) and the Cl contents of arc magmas (Métrich and Wallace, 2008). Other high-pressure processes in which mass transfer is influenced by chloride-rich fluids include mantle metasomatism, as recorded in fluid inclusions in mantle xenoliths (e.g., Anderson et al., 1984) and diamonds (e.g., Weiss et al., 2014, 2015), and granulite-facies metamorphism (e.g., Newton et al., 1998; Newton and Manning, 2010; Manning and Aranovich, 2014). Chloride-rich fluids are also associated with the formation of metasomatic features and ore deposition in mafic intrusions at a range of pressures (e.g., Clochiatti et al., 1981; Schiffries, 1982; Boudreau et al., 1986; Shmelev, 2011). Critical to assessing the extent and nature of metasomatism by chloride fluids in these high-pressure settings is knowledge of the solubility of mantle silicate minerals, including olivine, orthopyroxene and clinopyroxene, in aqueous saline solutions.

Here we report new experimental results on the solubilities of forsterite (Mg_2SiO_4), enstatite ($MgSiO_3$) and diopside ($CaMgSi_2O_6$) in H_2O-NaCl fluids. Forsterite and enstatite were studied at 1 GPa, 800 and 900 °C, to NaCl concentrations approaching halite saturation. Diopside solubility was determined in pure water at conditions ranging from 650 to 900 °C and 0.7 to 1.5 GPa, and in H_2O-NaCl solutions at 800 °C and 1 GPa at NaCl concentrations approaching halite saturation. The range of P-T conditions investigated is directly relevant to the lower crust and upper parts of the mantle wedge in convergent margin settings, at depths between about 25 and 40 km (pink shaded region in Fig. 1a). Phase relations for a model KLB-1 ultramafic composition in equilibrium with H_2O with reduced activity of 0.67, which is relevant for saline fluids, show that assemblages involving olivine, clinopyroxene, and orthopyroxene are stable at the conditions of our experiments (Fig. 1b), consistent with thermodynamic calculations in the system CaO-MgO-SiO_2-H_2O-NaCl (Newton and Manning, 2000b). In addition to the specific conditions investigated, the trends in solubility established by our experiments can aid in interpreting metasomatic processes at higher pressures and/or temperatures, such as the slab-mantle interface in subduction zones (Fig. 1a).

The new data fill key gaps in knowledge of mineral solubility at high pressure conditions. While there is an increasingly comprehensive data set on the solubilities in saline fluids of minerals associated with felsic or calc-silicate lithologies (Newton and Manning, 2000a, 2002b, 2006, 2007; Shmulovich et al., 2001, 2006; Wykes et al., 2008; Makhluf et al., 2016), studies of the mafic silicates are more limited (Newton and Manning, 2002a). Diopside solubility in pure H_2O has been investigated at relatively high P-T of 1100 and 1200 °C at 2 GPa and 1180 °C at 3 GPa (Eggler and Rosenhauer, 1978; Schneider and Eggler, 1986), as well as in pure H_2O and H_2O-NaCl solutions at intermediate to relatively low P-T: 650 °C and 0.2–0.75 GPa (Budanov and Shmulovich, 2000; Shmulovich et al., 2001). The P-T range of previous studies on diopside solubility are also shown on a cross-section of a model 'warm' subduction zone (Fig. 1a) for comparison. Our experimental conditions extend results in saline fluids from lower P and T and are over a wider P-T range than any previous single study in pure H_2O (Fig. 1b). Similarly, solubilities of enstatite + forsterite at mantle P-T have been investigated only in pure H_2O (Ryabchikov et al., 1982; Zhang and Frantz, 2000; Stalder et al., 2001; Mibe et al., 2002; Newton and Manning, 2002a), though mineral solubilities in the system MgO-SiO_2-H_2O-HCl have been investigated at low P-T and low total Cl (Frantz and Popp, 1979; Luce et al., 1985). Thus, the present work, in combination with previous solubility studies of wollastonite and quartz, allows direct comparison of the mobilities of Mg, Ca and Si in mafic and ultramafic systems, giving insight into the transport of these components in subduction zone/mantle wedge and lower crustal settings.

2. METHODS

Starting materials were single crystals of high-purity natural diopside and synthetic forsterite, enstatite and quartz, as well as reagent-grade NaCl, and ultrapure H_2O. The starting material used in diopside experiments were chips broken off of a single, gem-quality natural diopside crystal obtained from the mineral collection of the Department of Earth, Planetary, and Space Sciences at the University of California, Los Angeles. The diopside starting material was analyzed by electron probe microanalyzer (EPMA) and determined to be almost pure $CaMgSi_2O_6$, containing < 1 wt% other constituents (Table S1). Pieces from a large forsterite crystal grown by H. Takei by a flux-melt method (Takei and Hosoya, 1985) were used in our
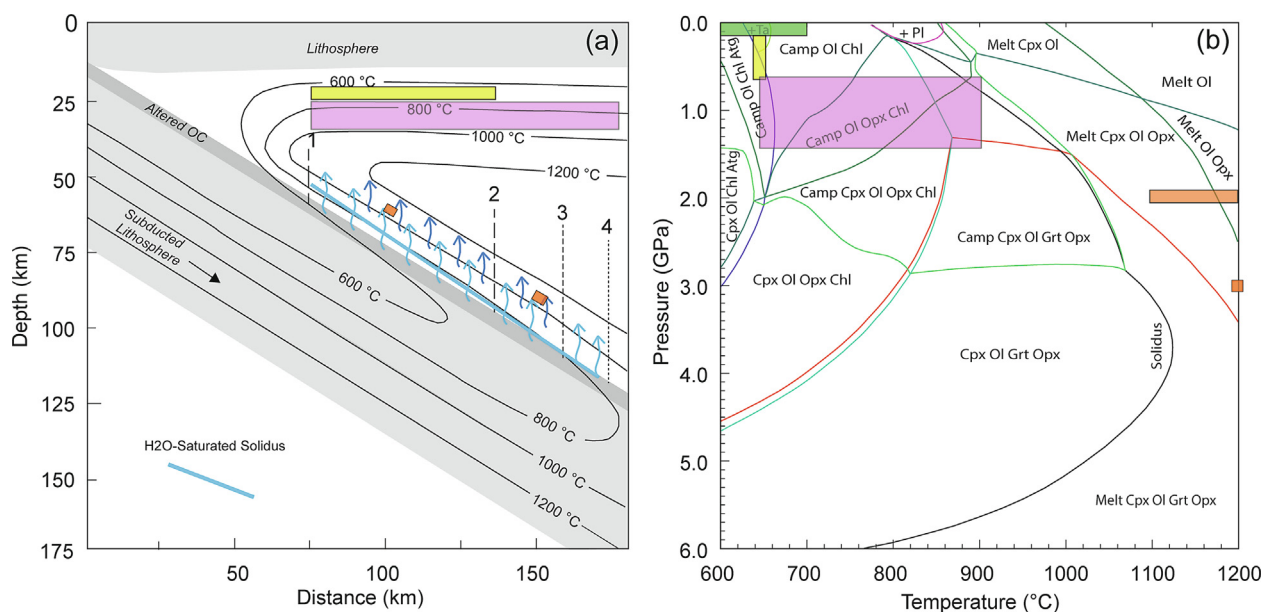
Fig. 1. The range of *P-T* conditions investigated in this study (pink shaded region) compared to previous work on diopside solubility, including the relatively low *P-T* data of Shmulovich et al. (2001) at 650 °C and 0.5 GPa and Budanov and Shmulovich (2000) at 650 °C and 0.2–0.75 GPa (yellow shaded region), and the much hotter and deeper conditions of the early experiments by Eggler and Rosenhauer (1978) (1200 °C and 2 GPa and 1180 °C and 3 GPa) and Schneider and Eggler (1986) (1100 °C and 2 GPa) (orange shaded regions). Also shown in (b) (in green) is the *P-T* range of previous experimental investigation of the solubility of MgO-SiO$_2$-H$_2$O minerals in chloride fluids (Frantz and Popp, 1979; Luce et al., 1985). (a) Cross section of a model 'warm' subduction zone showing isotherms and H$_2$O released from hydrous minerals in the slab (light blue arrows) and wedge (dark blue arrows). Figure modified from Till et al. (2012); their Fig. 8. Regions where experimental studies are relevant, shown as colored boxes (colors as described above). (b) Pressure-temperature phase diagram showing model ultramafic phase relations and locations of experimental studies (colors as described above). Abbreviations: clinopyroxene (Cpx), clinoamphibole (Camp), garnet (Grt), olivine (Ol), plagioclase (Pl), talc (Ta), antigorite (atg), chlorite (Chl), orthopyroxene (Opx). Phase relations calculated for simplified KLB-1 (Davis et al., 2009): Na$_2$O (0.24 mol%), CaO (2.82 mol%), FeO$_{tot}$ (5.88 wt%), MgO (50.53), Al$_2$O$_3$ (1.77 mol%), SiO$_2$ (38.47 mol%), O (0.096 mol%) H$_2$O (saturated, a$_{H2O}$ = 0.67), with 0.3 wt% Fe$_2$O$_3$ (Jennings and Holland, 2015). Constructed using PERPLE_X (v. 6.8.8, Connolly and Kerrick, 1987; Connolly, 2005), thermodynamic datafile DS6.22 (Holland and Powell, 2011), and activity-composition relations as follows: Cpx, Grt, Pl and Ol (Jennings and Holland, 2015), Camp (Green et al., 2016), Opx (Holland et al., 2013), Chl (White et al., 2014), Tlc (Holland and Powell, 1998), Atg (Padrón-Navarta et al., 2013). Melt composed of forsterite (foL), fayalite (faL), wollastonite (woL), albite (abL), sillimanite (silL), quartz (q8L), H$_2$O (h2oL) (Green et al., 2016). (For interpretation of the references to color in the figure legend, the reader is referred to the web version of this article.)

experiments. The pieces were ground and polished to a roughly cylindrical shape using Al$_2$O$_3$, SiC, and diamond abrasive paper, then cleaned with distilled H$_2$O in an ultrasonic bath. Single orthoenstatite crystals grown by a flux-melt method (Ito, 1975) were used. Rare crystals with visible flux inclusions were discarded. Small broken chips of Brazilian quartz (Manning, 1994; Newton and Manning, 2000a) were used as supplementary SiO$_2$ source in enstatite solubility experiments (see below).

In all experiments, forsterite, enstatite or diopside grains (∼0.2–4.5 mg) were placed in an inner Pt capsule (1.6 mm outer diameter), which was then crimped shut on both ends and punctured in two to four places to allow fluid penetration. The crimped and punctured capsules were placed in an outer capsule of 3.5 mm OD Pt tubing along with ultrapure H$_2$O ± NaCl ± quartz. The outer capsules were then sealed by carbon-arc welding. Weighing of capsules before and after welding revealed negligible (0.1 mg) average mass loss which is attributable entirely to sputtered Pt. Successful sealing of outer capsules was confirmed if no mass loss was observed after 1 hour in a 110 °C oven. In enstatite and forsterite experiments, masses of inner capsules, crys-

tals and any added SiO$_2$ (as quartz) were determined using a Mettler UMX2 ultramicrobalance (0.2 μg reproducibility). All other masses were determined using a Mettler MX3 microbalance (2 μg reproducibility).

Experiments were conducted in 19.05 mm or 25.4 mm end-loaded piston-cylinder apparatus. Capsules were loaded in a transverse (low temperature-gradient) orientation into furnace assemblies consisting of a cylindrical graphite heater, NaCl filler parts, and a concentric MgO and two-bore mullite thermocouple insulator (e.g., Manning and Boettcher, 1994). Temperature was monitored and controlled with Type-S thermocouples. Thermocouple EMF was not corrected for pressure effects. Pressure was monitored by a 12-inch Heise Bourdoun-tube pressure gauge. Experiments were conducted by the piston-out method of pressing and heating, wherein assemblies were pressed cold to a pressure 0.3 GPa below the final desired pressure, then heated to the final temperature. For example, in 1.0 GPa experiments, assemblies were initially pressurized to 0.7 GPa, followed by heating to run conditions (650–900 °C) at 50 °C/min. Thermal expansion of the NaCl pressure medium resulted in 1.0 GPa sample pressure at ∼600 °C

during the temperature ramp (i.e. piston-out). Oil pressure was subsequently bled to maintain pressure within 40 MPa (typically 15 MPa) of 1.0 GPa for the duration of the experiment. Calibration tests conducted in our laboratory show that this approach requires no friction correction and yield an accuracy of ±0.03 GPa.

Experiments were terminated by switching off the electrical heating power. Temperature dropped to 200 °C in <30 s in 25.4 mm assemblies, and about four times faster in 19.05 mm assemblies. Adhering NaCl from the furnace assembly was dissolved from the quenched capsule exterior. The capsule was then dried at 110 °C and weighed to check that no fluid was lost during the run. Capsules were punctured with a needle and dried at 115 °C for at least 1/2 h and reweighed as an additional check on H_2O content. In general, the apparent weight of H_2O after an experiment was slightly greater than the weight in; this is because there was inevitable minor loss of dissolved and finely particulate matter in the puncturing process. The starting H_2O weight was used in all solubility calculations.

After drying and weighing, the outer capsule was cut open with a razor blade to retrieve the inner capsule, which was then soaked in distilled water at 80 °C with a magnetic stirrer for 5–10 min, dried at 110 °C and reweighed. The process was repeated until attainment of constant mass, indicating removal of soluble NaCl. The weight change of the cleaned and dried inner capsule provided one measure of solubility. The contents of the inner capsule were then removed, examined optically under a binocular microscope, and weighed, giving a second solubility constraint. Selected run products were mounted and examined with a scanning electron microscope for composition and textural characteristics of residual crystals and quench material.

The composition of H_2O-NaCl fluids is presented as NaCl mole fraction ($X_{NaCl} = n_{NaCl}/(n_{NaCl} + n_{H_2O})$, where n is moles). Mineral solubility as determined from weight changes is presented in molality (m, mol/kg H_2O). Forsterite dissolution was generally congruent, and crystals could readily be extracted and weighed. Accordingly, m_{Fo} was simply determined from the mass loss of the crystal. In one experiment with pure H_2O, forsterite was found to dissolve incongruently to brucite + fluid. In this case, a brucite-absent fluid composition was calculated using the midpoint between crystal and inner-capsule mass loss, determining congruent solubility at a range of excess SiO_2 concentrations, and projecting to zero excess silica (see below).

Determination of enstatite solubility utilized a different method because of its incongruent dissolution producing forsterite. Forsterite generally formed a tough coating on enstatite grains, and the resulting crystal aggregate withstood post-run manipulation. It was therefore possible to obtain robust, separate weights of both the inner capsule and the crystal aggregate. We use the midpoint between these values for solubility calculations. We also conducted additional experiments, in which excess silica was introduced in the form of quartz. The quartz dissolved quickly and completely in the fluid to yield a starting solution closer to final equilibrium with the run products. Where sufficient
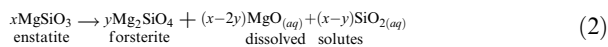
SiO_2 was added to prevent forsterite growth, a clean, uncoated enstatite crystal resulted. Although the final crystal weights in such runs had higher accuracy, we nevertheless report solubility as the midpoint between inner capsule and crystal weights to maintain consistency with the forsterite-saturated runs. At a given P, T and NaCl content, the fluid composition at the forsterite saturation point solubility was constrained by adding progressively greater SiO_2 concentrations (as quartz) and bracketing the fluid composition at which forsterite disappears from enstatite surfaces.

Diopside also dissolves incongruently at the conditions studied. As with enstatite and forsterite, the weight losses of inner capsules yield lower limits for diopside solubility, and upper limits are constrained by the weight loss of forsterite coated diopside crystals. Solubility results are reported as the midpoint between the two values, unless one of the weights was compromised. Runs with excess quartz were not conducted in the diopside solubility study.
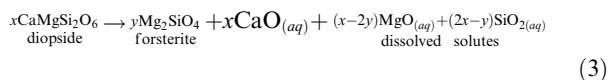
Incongruent dissolution complicates the determination of solubility by our methods. The mass of total dissolved solutes is readily obtained from the measured weight change, Δw. However, it is more desirable to know the absolute concentrations of the constituents derived from the dissolving solids, w_i, which are related to Δw by mass balance:

$$\Delta w = \sum_i w_i \tag{1}$$

where i is the number of solute constituents. Congruent dissolution constrains the solute stoichiometry to that of the dissolved mineral, so $i = 1$ and $w_i = \Delta w$, which leads to what can be termed a "true" solubility once any added solutes (e.g., SiO_2 in the present work) are taken into account. Incongruent dissolution involving a residual phase of different stoichiometry yields $i > 1$, and values of w_i cannot be determined from Δw alone. In molar form, for enstatite and diopside dissolution:

$$\underset{\text{enstatite}}{x MgSiO_3} \longrightarrow \underset{\text{forsterite}}{y Mg_2SiO_4} + \underset{\text{dissolved solutes}}{(x-2y)MgO_{(aq)} + (x-y)SiO_{2(aq)}} \tag{2}$$

and

$$\underset{\text{diopside}}{x CaMgSi_2O_6} \longrightarrow \underset{\text{forsterite}}{y Mg_2SiO_4} + x CaO_{(aq)} + \underset{\text{dissolved solutes}}{(x-2y)MgO_{(aq)} + (2x-y)SiO_{2(aq)}} \tag{3}$$

Eqs. (2) and (3) state that x moles of starting mineral are converted to y moles of forsterite and stoichiometrically determined amounts of dissolved oxide components (subscripted "(aq)"; these are solely stoichiometric entities for the purposes of mass balance and do not imply discrete solute species). Thus, incongruent dissolution prevents direct determination of solubility because, for each experiment, x and y are both unknown but only x–y (i.e., Δw in mass units) is measured.

We addressed this problem in two ways. First, we calculated an "apparent" solubility assuming that the concentration of $MgO_{(aq)}$ is zero (i.e., forsterite is insoluble), motivated by the very low Mg concentrations in equilibrium with forsterite in pure H_2O (Newton and

Manning, 2002a; this study). In this case, $x = 2y$, and the bulk solute stoichiometry is SiO_2 for enstatite and $CaSi_{1.5}$-O_4 for diopside.

More accurate solubility results can be obtained at conditions where high-precision determinations of the solubility of forsterite have been made; in the present study, this was at 800 and 900 °C, 1 GPa. At these conditions, forsterite dissolves congruently or very nearly so (see below). If we assume that solute Mg/Si in equilibrium with forsterite alone equals that with forsterite + enstatite, and that there is no complexing between the Mg and the other solutes (Si for enstatite; Si and/or Ca for diopside), then the dissolved Mg_2SiO_4 concentration in fluids with forsterite + enstatite or diopside is constrained. Thus, dissolution of x moles of starting mineral produces z moles of dissolved Mg_2SiO_4, $\frac{x}{2} - z$ moles of forsterite and $2z$ moles of $MgO_{(aq)}$, along with either $\frac{x}{2} + z$ moles of $SiO_{2(aq)}$ for enstatite (Eq. (2)), or x moles of $CaO_{(aq)}$ and $\frac{3x}{2} + z$ moles of $SiO_{2(aq)}$ for x diopside (Eq. (3)). This approach yields fluid compositions adjusted for known forsterite solubility. We therefore refer to concentrations calculated this way as "adjusted" solubilities.

Given the assumptions, the concentrations of dissolved oxide components in Eqs. (2) and (3) may be calculated from the weight change Δw by rewriting Eq. (1) as:

$$\Delta w = w_{Mg_2SiO_4(aq)} + w^*_{(aq)} \qquad (4)$$

where $w^*_{(aq)}$ is SiO_2 for enstatite and $CaSi_{1.5}O_4$ for diopside. For apparent solubilities, $w_{Mg_2SiO_4(aq)} = 0$; for adjusted solubility, $w_{Mg_2SiO_4(aq)}$ corresponds to independently determined forsterite solubility. In each case, Eq. (4) was solved for $w^*_{(aq)}$, which then allowed determination of the concentrations of individual oxide or element components for an experiment after accounting for any SiO_2 from added quartz.

3. EXPERIMENTAL RESULTS

3.1. Forsterite experiments

3.1.1. Textures

Results of forsterite solubility experiments are presented in Table 1 and Fig. 2. Run products from run Fo-09 in pure H_2O at 800 °C yielded a residual forsterite grain plus small (10–30 μm) flakes of newly grown crystals on the forsterite surface (Fig. 2a, b). Index of refraction and energy dispersive X-ray analyses indicate brucite (Fig. 2a, b). We interpret the brucite to result from slightly incongruent dissolution of forsterite in pure H_2O at these conditions. Additional experiments at the same conditions with added SiO_2 (Table 1) yielded no brucite, consistent with this interpretation. All other run conditions were free of brucite and yielded the starting forsterite crystal (Fig. 2c) ± halite cubes (depending on presence or absence of NaCl). The absence of brucite crystals on residual forsterite at 900 °C, and at 800 °C with NaCl, indicates congruent dissolution of forsterite. During H_2O-NaCl experiments, the starting crystals developed smooth surfaces and incipient facets (Fig. 2c), consistent with the high solubility calculated from mass loss relative to pure H_2O experiments.

3.1.2. Forsterite solubility

At 800 °C, run durations of ~1 day yielded consistently low solubilities (runs Fo-01 through Fo-05). Runs of ≥48 h yielded higher solubilities that were independent of duration within error. These runs are taken to reflect equilibrium and are reported in Table 1. Experiments conducted at 900 °C, $X_{NaCl} = 0.3$, and varying times showed that runs of 11–32 h yielded similar values. A shorter run (Fo-23, 6 h) likely had insufficient time to equilibrate, whereas a longer experiment (Fo-20, 70 hr) resulted in higher solubility (Fig. S1a) due to growth of new forsterite crystals in the outer capsule. These "vapor transport crystals" (Newton and Manning, 2006; Tropper and Manning, 2007; Antignano and Manning, 2008b) may nucleate and grow in longer runs as a consequence of convective mass transfer generated by the small temperature gradient. Such crystals cause apparent solubility to be higher than the equilibrium value. We limited run times at 900 °C to <70 h and carefully checked for the absence of these crystals.

Formation of brucite prevented direct determination of forsterite solubility in pure H_2O at 800 °C, 1 GPa. Instead it was found by linear extrapolation of the results of experiments with added SiO_2 (runs Fo-6, 7, 8, Table 1) to zero excess silica. Using the midpoint between solubility determined from the weight change of the forsterite crystal and the inner capsule yields $m_{Fo} = 0.0012(3)$ (parenthetical number is 1 standard deviation in final digit). Forsterite solubility in pure H_2O at 900 °C is 0.0046(1) molal. In H_2O-NaCl solutions, forsterite solubility increased with X_{NaCl} over the range of fluid compositions investigated, with a solubility of $m_{Fo} = 0.0424(10)$ molal at $X_{NaCl} = 0.471$ and 800 °C, a ~35-fold increase in solubility (Fig. 3). At 900 °C, forsterite solubility increases to $m_{Fo} = 0.0900(1)$ molal at $X_{NaCl} = 0.450$, an increase of ~20 times relative to the pure H_2O solubility. The solubility data at 800 and 900 °C and 1.0 GPa can be described by

$$m_{Fo} = 0.0013 + 0.0311X_{NaCl} + 0.0377X_{NaCl}^{1/2} \qquad (5)$$

at 800 °C, and

$$m_{Fo} = 0.0047 + 0.1212X_{NaCl} + 0.0446X_{NaCl}^{1/2} \qquad (6)$$

at 900 °C, with R of 0.998 and 0.999, respectively. These fit curves are plotted with the data in Fig. 3.

3.2. Enstatite experiments

3.2.1. Textures

Enstatite solubility experiments yielded run products with textures similar to those reported by Newton and Manning (2002a). Enstatite dissolved incongruently to forsterite + SiO_2-rich solute over the entire salinity range investigated (Fig. 2d). In each run product, euhedral, equant, granular forsterite crystals coat part or all of the enstatite crystal, depending on degree of dissolution; the external shape of the pseudomorphically replaced enstatite crystal retains that of the original crystal. Addition of SiO_2 yielded progressively smaller quantities of forsterite until only a subhedral enstatite crystal was found in the run products.

Table 1
Forsterite solubility experiment measurements at 1 GPa.

Expt. ID	T (°C)	t (h)	H$_2$O in (mg)	NaCl in (mg)	X_{NaCl}	qtz in (mg)	xl in (mg)	xl out (mg)	IC in (mg)	IC out (mg)	m_{Fo} (mol/kg H$_2$O)	Notes
Fo-09	800	48	36.462	0.000	0.000		4.2361	4.2187	61.1802	61.1694	–	Brucite
Fo-08	800	88	36.252	0.000	0.000	0.0343	0.4640	0.4568	68.7706	68.7674	0.0010(02)	Mid
Fo-07	800	84	36.204	0.000	0.000	0.1013	0.4707	0.4634	71.8352	71.8341	0.0008(04)	Mid
Fo-06	800	89	35.034	0.000	0.000	0.1825	0.3728	0.3684	66.6024	66.6026	0.0004(03)	Mid
Fo-15	800	69	35.203	41.524	0.050		1.4326	1.3768	57.9664	57.9129	0.0113(01)	
Fo-05	800	23	31.826	10.845	0.095		0.430	0.373	63.752	63.698	0.0127(06)	Short
Fo-12	800	97	34.580	19.774	0.150		4.5108	4.4066	58.7717	58.6699	0.0214(01)	
Fo-03	800	23	25.253	20.703	0.202		0.379	0.308	63.647	63.588	0.200(08)	Short
Fo-01	800	16	19.676	41.867	0.299		0.539	0.474	76.381	76.315	0.235(10)	Short
Fo-10	800	70	29.109	40.511	0.300		2.7313	2.6100	53.1093	52.9803	0.0296(01)	
Fo-13	800	49	30.046	41.867	0.300		2.4003	2.2662	60.2467	60.1194	0.0317(01)	
Fo-02	800	25	20.304	41.436	0.386		0.972	0.89	64.771	64.695	0.0287(10)	Short
Fo-11	800	65	20.458	59.144	0.471		3.4160	3.2940	57.7653	57.6480	0.0424(10)	
Fo-16	900	25	35.744	6.025	0.000		2.2660	2.2428	52.3451	52.3262	0.0046(01)	
Fo-21	900	44	35.750	6.108	0.050		3.8726	3.7684	63.6027	63.5010	0.0207(01)	
Fo-19	900	24	35.513	20.404	0.150		2.2427	2.0359	53.8015	53.5954	0.0414(01)	
Fo-23	900	6	30.044	41.771	0.300		1.0063	0.7546	53.8984	53.6444	0.0595(01)	Short
Fo-22	900	11	29.464	40.950	0.300		3.9463	3.6753	61.1608	60.8872	0.0654(01)	
Fo-24	900	20	29.745	41.375	0.300		3.5085	3.2460	60.0739	59.8003	0.0627(01)	
Fo-14	900	32	29.861	41.524	0.300		4.4067	4.1269	57.5063	57.2206	0.0666(01)	
Fo-20	900	70	30.088	41.840	0.300		2.7734	2.3144	59.1908	58.7254	0.1084(01)	vt
Fo-18	900	23	20.052	53.253	0.450		4.1264	3.8724	57.0409	56.7866	0.0900(01)	

Explanation: forsterite solubility (m_{Fo}) calculated from crystal weight change unless noted; "in" and "out" refer to weights before and after experiment; "xl", crystal; "mid", solubility is midpoint between values derived from crystal and capsule weight change; "vt", vapor transport; "short", insufficient run duration (see text). 1σ errors in weights given to three and four decimal places are respectively 0.002 and 0.0002 mg; errors in solubility (in parentheses) are propagated 1σ weighing errors in last decimal places.
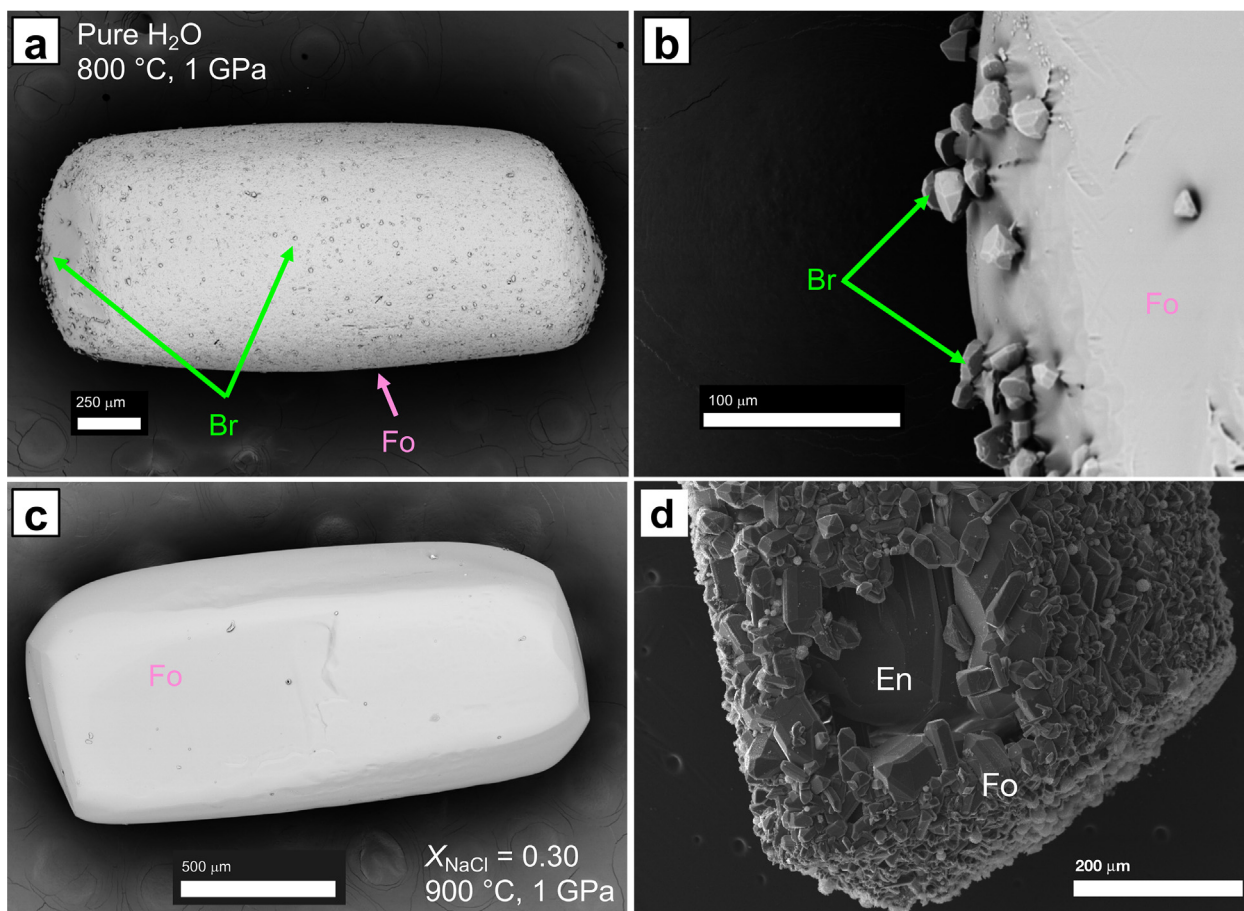
Fig. 2. Backscattered electron (BSE) images of run products from forsterite and enstatite solubility experiments. (a) Image of forsterite crystal from run Fo-09 in pure H_2O (800 °C, 1 GPa, Table 1) showing small brucite grains growing in pits on the surface as a result of incongruent dissolution. (b) Higher magnification image of Fo-09 showing detail of brucite crystals on the surface of the residual forsterite grain. (c) Forsterite crystal from run Fo-20 (900 °C, 1 GPa, $X_{NaCl} = 0.300$, Table 1) showing absence of brucite crystals; i.e., congruent dissolution. (d) BSE image of synthetic enstatite crystal partially converted to forsterite in run En-03 (Table 2). Note the hole in the forsterite crust, with smooth surface of original enstatite visible within. Larger forsterite grain size suggests the opening was present during the run. Higher BSE intensity spherules are Si-rich quench. Fo, forsterite; Br, brucite; En, enstatite.

3.2.2. Enstatite solubility

Results of enstatite solubility experiments are given in Table 2 and Fig. 4. As described above, apparent solubility in forsterite-saturated runs was estimated by assuming zero MgO in solution. The apparent enstatite solubility (as SiO_2) is shown in Fig. 4a in the upward pointing triangles. Solubilities obtained in the presence of fluid with excess SiO_2 and no forsterite are shown with downward pointing triangles in Fig. 4a. In the absence of other constraints, the fluid composition at a given X_{NaCl}, at which forsterite disappears from the surface, constrains the composition of a forsterite + enstatite-saturated fluid and lies between the two types of experimental result. Linear least-squares fits to the midpoints between forsterite-present and forsterite-absent runs give

$$m_{Si} = 0.297 - 0.0567 X_{NaCl} \tag{7}$$

and

$$m_{Si} = 0.499 + 0.0140 X_{NaCl} \tag{8}$$

at 800 and 900 °C respectively. The NaCl content of the fluid at 1.0 GPa and 800–900 °C has only a minor effect

on apparent solubility relative to values in pure H_2O from Newton and Manning (2002a).

Using our results on forsterite solubility in H_2O-NaCl, the adjusted solubility was calculated by combining Eqs. (4)–(6) to determine the fluid composition where forsterite was present (Table 2). Calculated concentrations confirm that dissolved Si is greater than dissolved Mg at all X_{NaCl} (Fig. 4b). With rising salt content, Mg increases significantly while Si declines slightly, regardless of temperature. The calculated dissolved Mg/Si (Fig. 4c) increases from relatively small values in pure H_2O to ∼0.3 at $X_{NaCl} = 0.3$ and is independent of temperature at 800–900 °C.

3.3. Diopside experiments

3.3.1. Textures

Run products from all diopside experiments consisted of the original diopside crystal with smaller forsterite crystals growing on the surface (Fig. 5). The forsterite occurs as ∼25–100 μm sub- to euhedral residual crystals on diopside grain surfaces (Fig. 5a–c). In some runs, loose crystals are
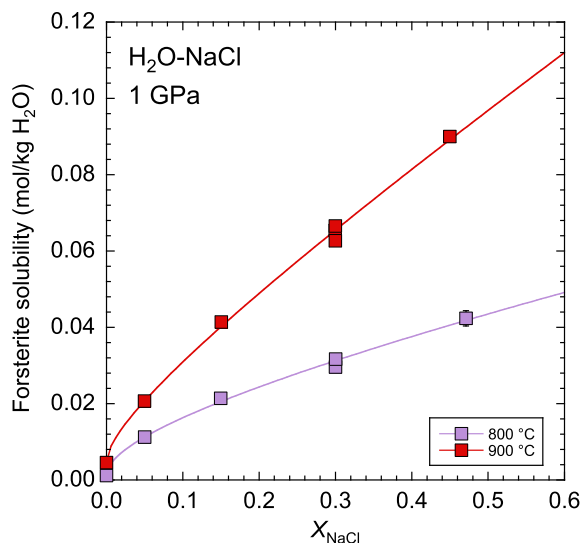
Fig. 3. Solubility of forsterite in molality (m_{Fo}) versus X_{NaCl} at 1 GPa and 800 °C (purple squares) and 900 °C (crimson squares). 2σ errors shown where larger than symbol size. Curves correspond to Eq. (5) (purple) and Eq. (6) (red) in the text, with the form $y = m_0 + m_1X_{NaCl} + m_2X_{NaCl}^{1/2}$. 1σ errors in the m_0-m_2 fit parameters are respectively 0.0011, 0.01, and 0.007 at 800 °C, and 0.0016, 0.016, and 0.011 at 900 °C. (For interpretation of the references to color in the figure legend, the reader is referred to the web version of this article.)

also present in inner capsules (Fig. 5d) and/or adhered to the inner capsule walls. This textural evidence indicates that diopside dissolves incongruently producing residual forsterite at all conditions investigated. In addition, blades and acicular sprays of wollastonite (in pure H_2O runs) and wollastonite plus enstatite (in H_2O-NaCl runs; Fig. 5c) occurred on grain surfaces, along with minor silica material, which forms as both small spheres ("fish roe"; Fig. 5d) and an amorphous coating on some crystal surfaces. These materials form a randomly distributed coating on the surface of residual diopside and forsterite crystals and walls of the inner and outer capsules. The morphology, random distribution, and abundance of the silica, wollastonite and enstatite, lead us to interpret these fine crystals and amorphous materials as quench phases, which were dissolved in solution at high *P-T* conditions. These types of quench products are typical of high *P-T* solubility studies of silicate minerals (e.g., Newton and Manning, 2006, 2007). The formation of enstatite quench crystals in run products from H_2O-NaCl experiments, but not in pure H_2O runs in this study, indicates a substantial increase in Mg^{2+} mobility in brines relative to pure H_2O, consistent with the results of our enstatite solubility experiments (Table 2). The overall mass of quench materials is small and can be neglected.

3.3.2. Diopside solubility

Results from diopside experiments are given in Table 3. Experiments in pure H2O at 700 °C and varying times showed that solubilities achieved by 10 h were identical within error to solubilities at 40 h (Fig. S1b); it is therefore assumed that run times ≥10 h were sufficient to attain equi-

librium. SEM analyses revealed that in several experiments small diopside crystals nucleated and grew in the outer capsule or on the walls of the inner capsule. These are interpreted as vapor-transport crystals as in forsterite experiments; any runs showing evidence for these crystals were discarded.

Experiments in pure H_2O were conducted from 0.7 to 1.5 GPa and 650–900 °C. The apparent solubility of diopside ($m_{Di\ app}$) increases with increasing pressure and temperature. At 1 GPa, the apparent solubility increases from 0.0060(5) molal at 650 °C to 0.0141(8) molal at 900 °C (Fig. 6a). At 800° C and 0.7–1.5 GPa, apparent solubility increases from 0.0028(6) to 0.0208(6) molal (Fig. 6b). A least-squares fit to these data yields the equation:

$$\log m_{Di\ app} = -1.269 - \frac{1758}{T} + 0.910P \qquad (9)$$

where *T* is in K and *P* is in GPa. Average absolute deviation between data and fit is 9% relative for all experiments, excepting gdi15 at 800 °C, 0.7 GPa (Table 3), which was not included in the fitting because the midpoint solubility could not be obtained (Table 3). The fit yields higher solubility than measured at 1.5 GPa, 800 °C. A functional form that is linear in *P* would improve the fit, but Eq. (9) reproduces previous work at higher *P* and *T* reasonably well (see Section 4.2 below). We therefore chose to retain the form of the fit equation.

We investigated the influence of NaCl on diopside solubility at 800 °C and 1 GPa (Fig. 7a). Fig. 7a shows that apparent diopside solubility is significantly enhanced with increasing NaCl concentration, rising from 0.0107(6) molal in pure H_2O and then leveling off to a maximum of 0.1761 (37) molal ($X_{NaCl} = 0.5$), near halite saturation ($X_{NaCl} = 0.62$, Aranovich and Newton, 1996). A least-squares fit to the variation of diopside apparent solubility ($m_{Di\ app}$) with X_{NaCl} at 800 °C, 1 GPa, yields the equation:

$$m_{Di\ app} = 0.0049 + 0.0716X_{NaCl} + 0.1994X_{NaCl}^{1/2} \qquad (10)$$

(R = 0.995) (Fig. 7a).

At 800 °C, 1 GPa, the solute composition in H_2O-NaCl fluid coexisting with diopside + forsterite can be estimated using Eqs. (4) and (5). The procedure outlined in §2 was followed to obtain Si, Ca and Mg concentrations as a function of X_{NaCl} (Fig. 7b). The solutions are enriched in Si relative to Ca over the full compositional range. Mg concentrations are lower than Si and Ca, as required by the residual forsterite coating. Calculated molar Si/Ca, Mg/Si and Ca/Mg are nearly constant at ~1.8, 0.33 and 1.7, respectively, in all NaCl-bearing solutions.

4. DISCUSSION

4.1. Accuracy of calculated solute concentrations

Apparent solubilities of enstatite and diopside were calculated assuming that forsterite is insoluble ($m_{MgO_{(aq)}} = 0$), whereas adjusted solubilities account for forsterite's solute contribution. In pure H_2O, where forsterite solubility was found to be very low (Fig. 3), the difference between apparent and adjusted solubilities is small. In the case of enstatite,

Table 2
Results of enstatite solubility experiments.

Expt. ID	T (°C)	P (GPa)	time (h)	H_2O in (mg)	NaCl in (mg)	X_{NaCl}	qtz in (mg)	xl in (mg)	xl out (mg)	IC in (mg)	IC out (mg)	Apparent solubility (mol/kg H_2O)	m_{Si} (mol/kg H_2O)	m_{Mg} (mol/kg H_2O)	Notes
En-03	800	1	20	30.702	11.190	0.101		1.5630	1.0221	68.928	68.461	0.273(12)	0.251(12)	0.033(06)	+fo
En-11	800	1	70	32.003	11.257	0.098	0.5346	2.4060	2.3099	54.541	54.468		0.304(02)	0.026(02)	-fo
En-01	800	1	7	28.865	23.333	0.199		1.4212	0.9723	67.914	67.505	0.247(07)	0.215(09)	0.049(08)	+fo
En-17	800	1	67	27.059	22.568	0.204	0.3294	1.2831	1.1657	59.395	59.301	0.268(04)	0.234(07)	0.049(08)	+fo
En-15	800	1	69	31.875	25.919	0.200	0.5071	0.9757	0.7701	60.748	60.587		0.322(04)	0.057(04)	-fo
En-08	800	1	68	19.458	27.032	0.300		1.2486	0.9588	56.795	56.517	0.243(03)	0.201(08)	0.063(10)	+fo
En-09	800	1	71	20.108	27.607	0.297	0.3100	1.4939	1.3844	56.646	56.548		0.308(02)	0.051(02)	-fo
En-02	800	1	20	21.979	34.319	0.325		1.9710	1.6003	87.257	86.978	0.246(20)	0.202(21)	0.066(11)	+fo
En-06	900	1	14	31.01	11.145	0.100	0.5379	1.2610	nd	49.872	49.496	0.490(02)	0.449(02)	0.062(08)	+fo
En-07	900	1	14	32.529	11.762	0.100	0.9023	1.1467	0.9682	48.976	48.823		0.512(02)	0.051(02)	-fo
En-16	900	1	20	27.068	19.341	0.180	0.4494	1.4160	1.0204	63.852	63.500	0.506(08)	0.445(11)	0.091(11)	+fo
En-13	900	1	19	30.212	23.840	0.196	0.7289	0.8911	0.5751	66.715	66.392		0.507(01)	0.105(01)	-fo
En-05	900	1	12	15.028	20.641	0.297		1.8366	1.3436	63.594	63.183	0.501(26)	0.413(28)	0.130(15)	+fo
En-10	900	1	22	20.514	28.012	0.296	0.5139	2.5713	2.4060	61.966	61.790		0.500(01)	0.083(01)	-fo
En-04	900	1	13	20.997	28.285	0.293	0.5026	1.6728	1.4654	66.869	66.625		0.505(05)	0.107(05)	-fo

Explanation: Abbreviations and weight errors as in Table 1, except: "nd", not determined; "+fo", forsterite present; "-fo", forsterite absent. All solubility entries are midpoints between those from crystal and inner capsule weight changes, except En-06 for which xl out could not be weighed. Where forsterite was present, apparent solubility assumes solute is SiO_2 only, and m_{Si} and m_{Mg} were calculated using Eqs. (3), (5) and (6) (see text). Numbers in parentheses are 1σ errors in final digits calculated numerically by Monte Carlo simulation (10,000 trials) based on weighing errors and errors in Eqs. (5) and (6); 1σ errors in X_{NaCl} are 2 to 4×10^{-5} and are omitted.

apparent solubilities at 800 and 900 °C, 1 GPa, are respectively 0.296 ± 0.001 m and 0.497 ± 0.001 m, compared to adjusted solubilities of 0.294 ± 0.002 m and 0.495 ± 0.002 m. For diopside, apparent Ca solubility at 800 °C and 1 GPa is 0.0107 ± 0.006 m vs. adjusted solubility of 0.0095 ± 0.0012 m. (Si solubility is 1.5 times these values; errors are 1σ). It is evident that the adjustment leads to smaller values, but the differences are so small that, for pure H_2O, apparent solubilities are adequate for quantifying changes with P and T, and comparing results among different studies. However, differences between apparent and adjusted solubilities increase with increasing concentration and increasing forsterite solubility, so where NaCl is pre-

sent in solution, adjusted solubilities are essential for determination of the fluid composition.

We can also evaluate the assumptions underlying the calculation of adjusted solubility. The assumption that the dissolved Mg concentration is fixed and corresponds to that at forsterite saturation is required to compute adjusted fluid compositions in enstatite + forsterite and diopside + forsterite experiments. Two factors could invalidate the assumption. First, it is possible that the dissolved Mg concentration in equilibrium with forsterite alone is non-negligibly different from that with forsterite and enstatite or diopside. Because the latter equilibrium point dictates higher SiO_2 activity and lower MgO activity than equilibrium with forsterite alone, the MgO concentration could be lower, and SiO_2 higher, where two minerals are present. The second factor is that interaction between dissolved SiO_2, Mg and Ca are possible via metal-silicate complexing (e.g., Sverjensky et al., 1997; Huang and Sverjensky, 2019).

The assumptions can be evaluated in the case of enstatite by comparing calculated Mg concentrations with those in comparatively silica-rich solutions that resulted in enstatite without a forsterite coating, which allows direct determination of the Mg concentration. Fig. 8 compares Mg concentrations in equilibrium with only forsterite and only enstatite. At any given X_{NaCl}, Mg concentration in equilibrium with forsterite + enstatite lies on the forsterite curves. The lack of systematic deviation of the enstatite-only data either above or below the curves indicates that the Mg concentrations in fluids coexisting with forsterite alone, enstatite alone, or forsterite + enstatite are similar within our detection limits. This supports the accuracy of the calculated fluid compositions in enstatite + forsterite experiments. In addition, thermodynamic data on Mg-silicate complexing, as represented by the aqueous species $Mg(HSiO_3)^+$, imply negligible concentrations at 1 GPa, 800 and 900 °C, and X_{NaCl} up to $\sim$0.15 (Sverjensky et al., 2014; Huang and Sverjensky, 2019). We take this as sufficient to assume accuracy of the derived fluid compositions in diopside + forsterite experiments, though a similar test was not performed.
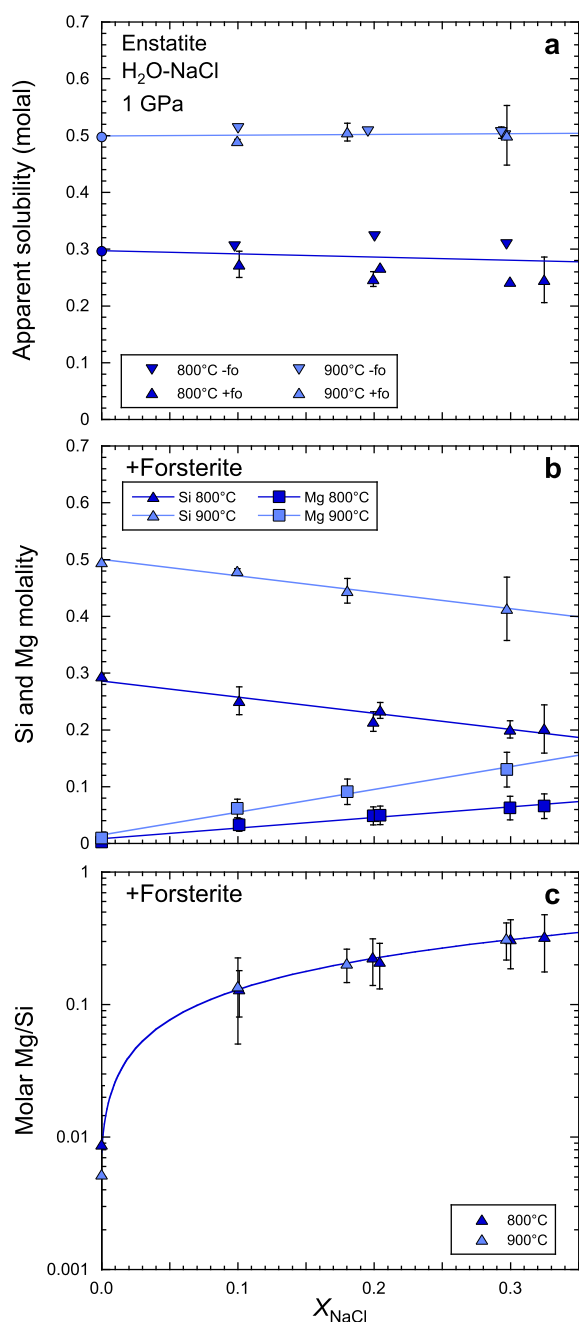

Fig. 4. (a) Apparent solubility of enstatite at 800 and 900 °C, 1 GPa, versus NaCl mole fraction. Upward pointing triangles represent apparent solubility in the presence of forsterite, which is assumed to be insoluble (see text). Downward pointing triangles are true solubility in the absence of forsterite, in experiments to which excess Si was added. The two types of experiments respectively constrain lower and upper bounds on the solubility of enstatite alone at Si concentration just sufficient to suppress forsterite. Lines are linear best fits to the midpoints between these bounds. Values at $X_{NaCl} = 0$ from Newton and Manning (2002a). (b) Calculated molalities of Si and Mg versus X_{NaCl} in enstatite + forsterite saturated fluids. Solute concentrations derived using results of forsterite solubility experiments (Eqs. (5) and (6); see text). Lines are linear best fits to the results. (c) Molar Si/Mg versus X_{NaCl}. The blue curve is a best fit to the combined data: $Mg/Si = 0.00825 + 0.6956 \; X_{NaCl} + 0.1685 \; X_{NaCl}^2$. In all panels, 2σ errors are shown where larger than symbol size. (For interpretation of the references to color in the figure legend, the reader is referred to the web version of this article.)
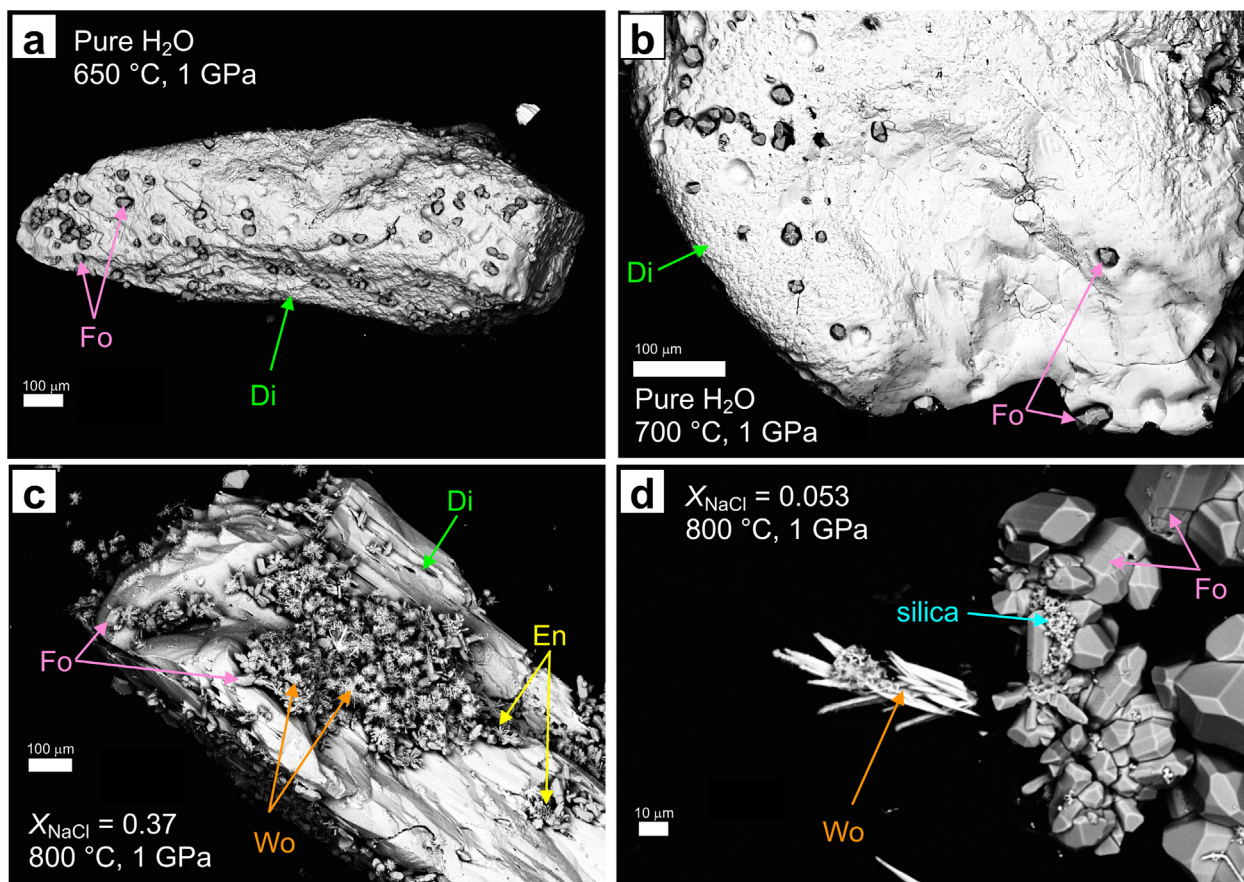
Fig. 5. Backscattered electron (BSE) images of run products from diopside solubility experiments showing textures of residual diopside and forsterite crystals, as well as quench phases (wollastonite and enstatite). (a) Image of diopside crystal from run gdi5 (650 °C, 1 GPa, pure H_2O) showing subhedral forsterite grains growing in pits on the surface. (b) Image of diopside crystal from run gdi3 (700 °C, 1 GPa, pure H_2O) showing details of forsterite grains growing in pits on the surface. (c) Diopside crystal from run db4 (800 °C, 1 GPa, $X_{NaCl} = 0.317$) with forsterite crystals partially covered by acicular sprays of quench wollastonite and enstatite. (d) Materials retrieved from the inner capsule of run db6 (800 °C, 1 GPa, $X_{NaCl} = 0.496$): quench wollastonite blades, amorphous silica spheres and residual forsterite (diopside crystal not shown). Fo: forsterite; Di: diopside; Wo: wollastonite; En: enstatite.

4.2. Comparison to previous results

4.2.1. Forsterite and enstatite

Limited data are available for direct comparisons at the P and T of this study. The solubility behavior of CaO-MgO-SiO_2-H_2O minerals was investigated in previous studies, with and without HCl, at lower P and T (e.g., Hemley et al., 1977a,b; Frantz and Popp, 1979; Luce et al., 1985), but we are not aware of previous studies of forsterite or enstatite solubility in NaCl-bearing H_2O. Forsterite and enstatite solubilities in pure H_2O have been more extensively investigated, but typically at higher P and T near the wet solidus in the system forsterite-quartz-H_2O. An exception is the study by Newton and Manning (2002a), who found that forsterite solubility in pure H_2O was below their detection limit at the conditions investigated here. Our new results with improved detection limits and precision quantify forsterite solubility in pure H_2O for the first time.

Experiments by Newton and Manning (2002a) showed that enstatite dissolved incongruently to forsterite + fluid in pure H_2O at 800 and 900 °C, 1 GPa. Similar behavior was observed by Ryabchikov et al. (1982) at 3 GPa, 900 °C. Incongruent dissolution appears to persist to higher T at these pressures (e.g., Nakamura and Kushiro, 1974; Zhang and Frantz, 2000); however, the data of Stalder et al. (2001) and Mibe et al. (2002) suggest congruent enstatite dissolution at ≥ 6 GPa. A transition from incongruent to congruent dissolution at 3–6 GPa implies increasing Mg/Si in enstatite + forsterite saturated fluid with pressure (e.g., Stalder et al., 2001; Kawamoto et al., 2004). Combining our results with previous work confirms this trend: at 1 GPa, 800 and 900 °C, we find Mg/Si of 0.009 and 0.020, respectively. At 3 GPa, 900 °C, Mg/Si = 0.33 (Ryabchikov et al., 1982), while at 6 GPa it is ~1 (Stalder et al., 2001). The results and trends in pure H_2O differ from a recent determination of enstatite + forsterite solubility in H_2O at 800 °C, 1 GPa. Using a diamond-trap technique, Tiraboschi et al. (2018) found $m_{Si} = 0.22$, $m_{Mg} = 0.28$, and Mg/Si = 1.3. While m_{Si} agrees reasonably well with Newton and Manning (2002a), Mg and Mg/Si differ substantially from our adjusted solubilities ($m_{Mg} = 0.0026$ m and Mg/Si = 0.0088). The datum of Tiraboschi et al. is also

Table 3
Results of diopside solubility experiments.

Expt. ID	T (°C)	P (GPa)	t (h)	H$_2$O in (mg)	H$_2$O out (mg)	NaCl in (mg)	X_{NaCl}	xl in (mg)	xl out (mg)	IC in (mg)	IC out (mg)	Apparent m_{Di} (mol/kg H$_2$O)	Adjusted m_{Si} (mol/kg H$_2$O)	Adjusted m_{Ca} (mol/kg H$_2$O)	Adjusted m_{Mg} (mol/kg H$_2$O)	Notes
gdi5	650	1.0	10	36.112	36.134			0.886	0.855	60.280	60.248	0.0060(5)				
gdi3	700	1.0	4	35.936	35.960			2.089	2.055	65.984	65.948	0.0067(4)				
gdi2	700	1.0	8	35.775	35.822			1.113	1.078	66.888	66.860	0.0060(6)				
di4	700	1.0	12	36.323	31.498			0.337	0.304	77.413	77.387	0.0056(5)				
di9	700	1.0	18	35.898	35.941			0.533	0.486	51.191	51.151	0.0083(6)				vt
di6	700	1.0	24	35.983	33.029			3.419	3.384	75.178	75.147	0.0063(5)				
di3	700	1.0	40	36.539	36.575			2.471	2.433	64.841	64.810	0.0065(6)				
di7	750	1.0	21	35.720	35.734			1.009	0.962	59.378	59.336	0.0085(5)				
gdi15	800	0.7	20	nd	21.677			0.425	0.416	44.528	-	0.0028(6)				xl only
gdi7	800	1.0	10	35.660	35.720			1.017	0.958	57.106	57.053	0.0107(6)	0.0155(10)	0.0095(12)	0.0026(22)	
db11	800	1.0	96	nd	36.010	2.148	0.018	1.630	1.480	74.850	74.716	0.0270(10)	0.0374(16)	0.0203(17)	0.0139(30)	
db6	800	1.0	12	38.366	38.362	6.931	0.053	0.506	0.186	72.955	72.733	0.0483(51)	0.0673(76)	0.0372(53)	0.0232(41)	
db8	800	1.0	15	36.305	36.601	12.836	0.098	1.304	0.871	78.881	78.532	0.0737(46)	0.1033(71)	0.0581(53)	0.0323(54)	
db10	800	1.0	12	26.826	26.937	22.235	0.204	1.624	1.067	81.165	80.801	0.1174(142)	0.1652(216)	0.0937(148)	0.0493(80)	
db4	800	1.0	10	28.752	28.791	43.218	0.317	2.134	1.464	78.816	78.277	0.1483(90)	0.2014(136)	0.1127(101)	0.0647(105)	
db5	800	1.0	10	20.296	20.330	64.831	0.496	2.096	1.555	83.020	82.516	0.1761(37)	0.2449(65)	0.1344(82)	0.0866(148)	
gdi13	800	1.2	10	35.375	34.208			0.413	0.326	52.863	52.791	0.0154(10)				
gdi12	800	1.5	15	35.318	33.755			0.832	0.720	54.050	53.947	0.0208(6)				
gdi8	850	1.0	16	36.666	36.695			0.487	0.408	54.570	54.515	0.0125(14)				
gdi10	850	1.0	10	nd	35.839			0.681	0.611	53.117	53.063	0.0118(10)				
gdi9	900	1.0	10	31.380	26.951			1.144	1.075	53.665	53.605	0.0141(8)				

Explanation: Abbreviations and weight and solubility errors as in Tables 1 and 2, except: "xl only" indicates solubility determined by weight change of the crystals because inner capsule weight could not be determined due to partial welding to outer capsule. All solubility entries are midpoints between crystal and inner capsule results using "H$_2$O in" unless not determined. Apparent solubility calculated assuming solute is CaSi$_{1.5}$O$_4$; m_{Si}, m_{Ca} and m_{Mg} are calculated using Eqs. (4) and (5) (see text). Numbers in parentheses are 1σ errors in final digits calculated numerically by Monte Carlo simulation (10,000 trials) based on weighing errors and error in Eq. (5); 1σ errors in X_{NaCl} are 2 to 4×10^{-5} and are omitted.
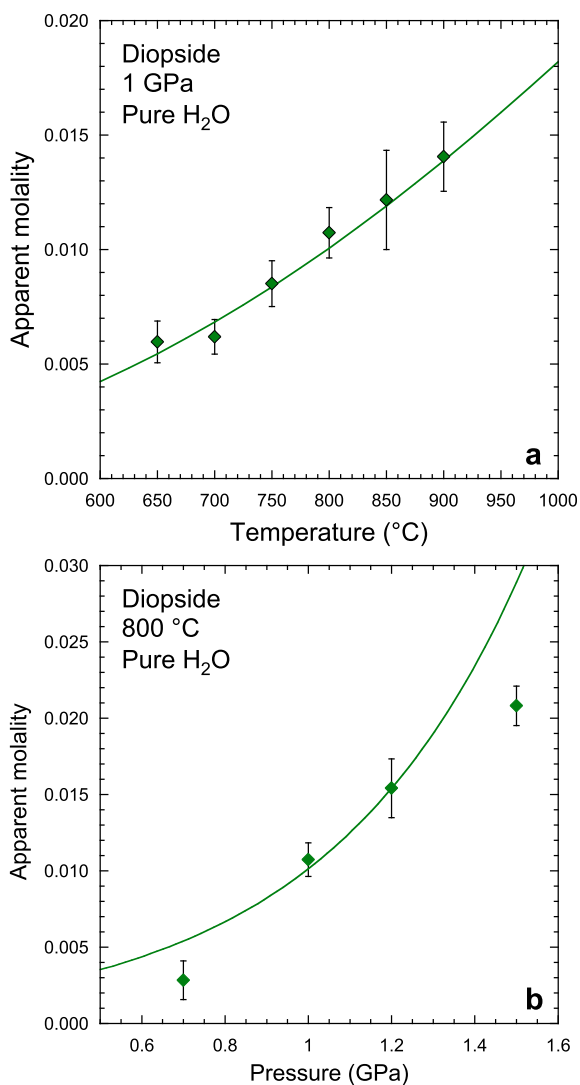
Fig. 6. Apparent solubility of diopside in pure H_2O as function of temperature at 1 GPa (a) and of pressure at 800 °C (b). Curves calculated from Eq. (9). 2σ errors are shown where larger than symbol size.
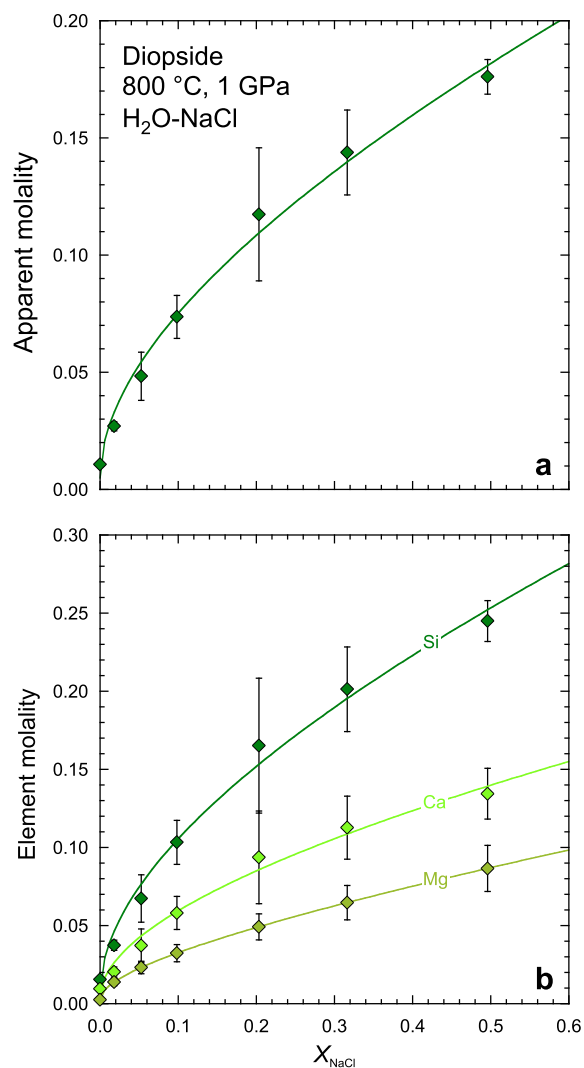

Fig. 7. (a) Apparent solubility of diopside with increasing X_{NaCl} at 1 GPa and 800 °C. Curve calculated from Eq. (10). (b) Si, Ca and Mg solubilities with increasing X_{NaCl} at 1 GPa and 800 °C. 2σ errors are shown where larger than symbol size.

inconsistent with the trend of rising Mg/Si with pressure in that it is greater than values at 3–6 GPa determined by Ryabchikov et al. (1982) and Stalder et al. (2001). We do not know the source of this discrepancy.

Increasing NaCl concentration has the same effect as pressure in pure H_2O (Fig. 4c). For example, the trends in Fig. 4c imply that Mg/Si of 900 °C, 3 GPa (0.33) is attained at $X_{NaCl} = 0.38$ at 1 GPa.

Our results can also be compared to solubilities calculated using high P-T thermodynamic data for aqueous species in the Deep Earth Water (DEW) model (Sverjensky et al., 2014) and the EQ36 package (Wolery, 1992; Wolery and Daveler, 1992). At 800 °C, forsterite is predicted to dissolve incongruently to brucite at $X_{NaCl} = 0$ to 0.014, but congruently at higher X_{NaCl}; and predicted solubility in pure H_2O (0.0012 molal) agrees well with that measured (0.0012 molal). However, a substantially smaller

dependence on NaCl is predicted. For example, at X_{NaCl} ~ 0.05 (3 molal) measured forsterite solubility is 0.011 molal, but the predicted value is about 10 times lower (0.0012), and the disparity grows with increasing NaCl. Enstatite is predicted to dissolve incongruently at 800 °C in pure H_2O and H_2O-NaCl solutions and there is good agreement with the measured values in pure H_2O, but solubility is again significantly under predicted as NaCl is added. These results imply that thermodynamic data for Mg-chloride and Na-silicate species may need revision.

4.2.2. Diopside

Early experiments investigated diopside solubility at very high P-T in H_2O. Eggler and Rosenhauer (1978) determined the solubility of diopside in H_2O by phase equilibria, and reported that diopside dissolved stoichiometrically (i.e., congruently) at 1200 °C, 2.0 GPa and 1180 °C, 3.0 GPa; resulting in solubilities of 0.48 ± 0.07 and 0.5 ± 0.07 molal, respectively. Schneider and Eggler (1986) found that, in
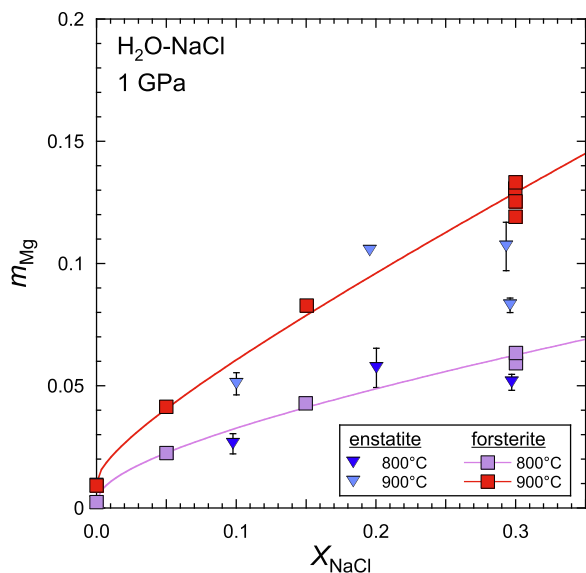
Fig. 8. Comparison of Mg concentration in H_2O-NaCl solutions coexisting with forsterite and enstatite at 1 GPa, 800 and 900 °C. Forsterite data are shown in purple (800 °C) and red (900 °C) squares. Purple and red curves calculated from Eqs. (5) and (6). Downward pointing dark blue and light blue triangles correspond to the Mg content at 800 and 900 °C in experiments in which only enstatite was present as a run product (Table 2). 2σ errors shown where larger than symbol size. The similarity of the Mg concentrations in fluids coexisting with enstatite and forsterite supports assumptions used to derive the adjusted compositions of fluids coexisting with forsterite + enstatite. (For interpretation of the references to color in the figure legend, the reader is referred to the web version of this article.)

H_2O vapor at 1100 °C, 2.0 GPa, diopside dissolved incongruently to forsterite and fluid. They obtained an apparent solubility of 0.14 molal by weight loss methods (no error was reported). The discrepancies between these studies may be due to differences in experiment durations – Eggler and Rosenhauer (1978) run durations were 1.17 and 2.25 h, while Schneider and Eggler (1986) run durations were 24 h – and/or from differences in methods used to determine solubility. Comparisons of the 2 GPa experiments from both studies with the results of this work (Fig. 9a) show excellent agreement between our Eq. (9) and the Schneider and Eggler (1986) datum, but not that of Eggler and Rosenhauer (1978), suggesting that shorter experiment durations and the phase equilibrium approach yielded results of low accuracy. The good agreement between our Eq. (9) and the data of Schneider and Eggler (1986) lends confidence to the accuracy of extrapolation of our results to higher pressures and temperatures than those investigated directly, and support our choice of run durations.

Two more recent studies focused on diopside solubility at P and T relevant to crustal metamorphism. One reported experiments at 650 °C, 0.2–0.75 GPa, including investigation of diopside solubility in pure H_2O and in H_2O-NaCl solutions (Budanov and Shmulovich, 2000). Another investigated diopside solubility at 650 °C and 0.5 GPa in pure water and in a 53.22 mol% NaCl solution (Shmulovich

et al., 2001). Both studies found that diopside dissolved incongruently at all investigated conditions. The apparent diopside solubilities in pure H_2O from Budanov and Shmulovich (2000) and Shmulovich et al. (2001) are compared with our results at 0.5 GPa in Fig. 9b, and at 650 °C in Fig. 9c. Fig. 9b shows that our Eq. (9) predicts that apparent solubility lies between the results of the two studies. Comparisons at 650 °C and a range of pressures (Fig. 9c) reveal that while our data agree well with the Budanov and Shmulovich (2000) datum at 0.5 GPa, the 0.7 GPa experiment from their study yielded a higher $m_{Di\ app}$ than predicted by Eq. (9). This could be due to undetected vapor transport crystals in the 0.7 GPa experiment of Budanov and Shmulovich (2000), which would result in an erroneously high weight loss and solubility.

Direct comparisons of the apparent solubility of diopside in H_2O-NaCl solutions from this study with those of Budanov and Shmulovich (2000) are hampered by the different P-T conditions investigated. However, Fig. 9d shows that $m_{Di\ app}$ increases with increasing X_{NaCl}, at all conditions from both studies. Moreover, comparison of our results with the 0.2 and 0.5 GPa data of Budanov and Shmulovich (2000) reveals that the form of the dependence of apparent solubility on X_{NaCl} is similar. In contrast, the results of Budanov and Shmulovich (2000) at 0.75 GPa imply a smaller relative increase with X_{NaCl}. However, this is likely a consequence of their very high apparent diopside solubility in pure H_2O at this P and T. If the value predicted from our Eq. (9) is substituted, the trend at 0.75 GPa is similar to that at other conditions (dashed red line in Fig. 9d). This further supports the suggestion that the 650 °C, 0.75 GPa experiment of Budanov and Shmulovich (2000) may have had undetected vapor transport crystals.

At 800 °C, 1 GPa, the DEW model predicts that diopside dissolves incongruently to merwinite and forsterite in pure H_2O, and to forsterite in H_2O-NaCl solutions. Predicted Si, Ca, and Mg concentrations in equilibrium with diopside + forsterite in pure H_2O and H_2O-NaCl are all lower than measured.

4.3. Dependence of solubility on solvent composition

The results at 800 °C, 1 GPa, allow comparison of the relative roles of H_2O and NaCl on the solubilities of key CaO-MgO-SiO$_2$ minerals, based on data from this study and that of Newton and Manning (2000a, 2006) on quartz (SiO$_2$) and wollastonite (CaSiO$_3$). Wollastonite and quartz dissolve congruently at these conditions. Similar behavior of forsterite means that dissolved molar Mg/Si is fixed at 2 in solutions formed by dissolving this mineral alone. Using the molality scale (Fig. 10a), forsterite solubility rises with NaCl, but is significantly lower than that of the other minerals shown. In the case of diopside, Si, Ca and Mg molalities all rise with NaCl (Fig. 7b), and – with the exception of pure H_2O – molar element ratios are nearly constant (Table 3). Comparing diopside to other minerals using Si, the most abundant solute, reveals a trend of increasing molality lying between the trends for forsterite and wollastonite. For enstatite, the behavior of Si and Mg differ:
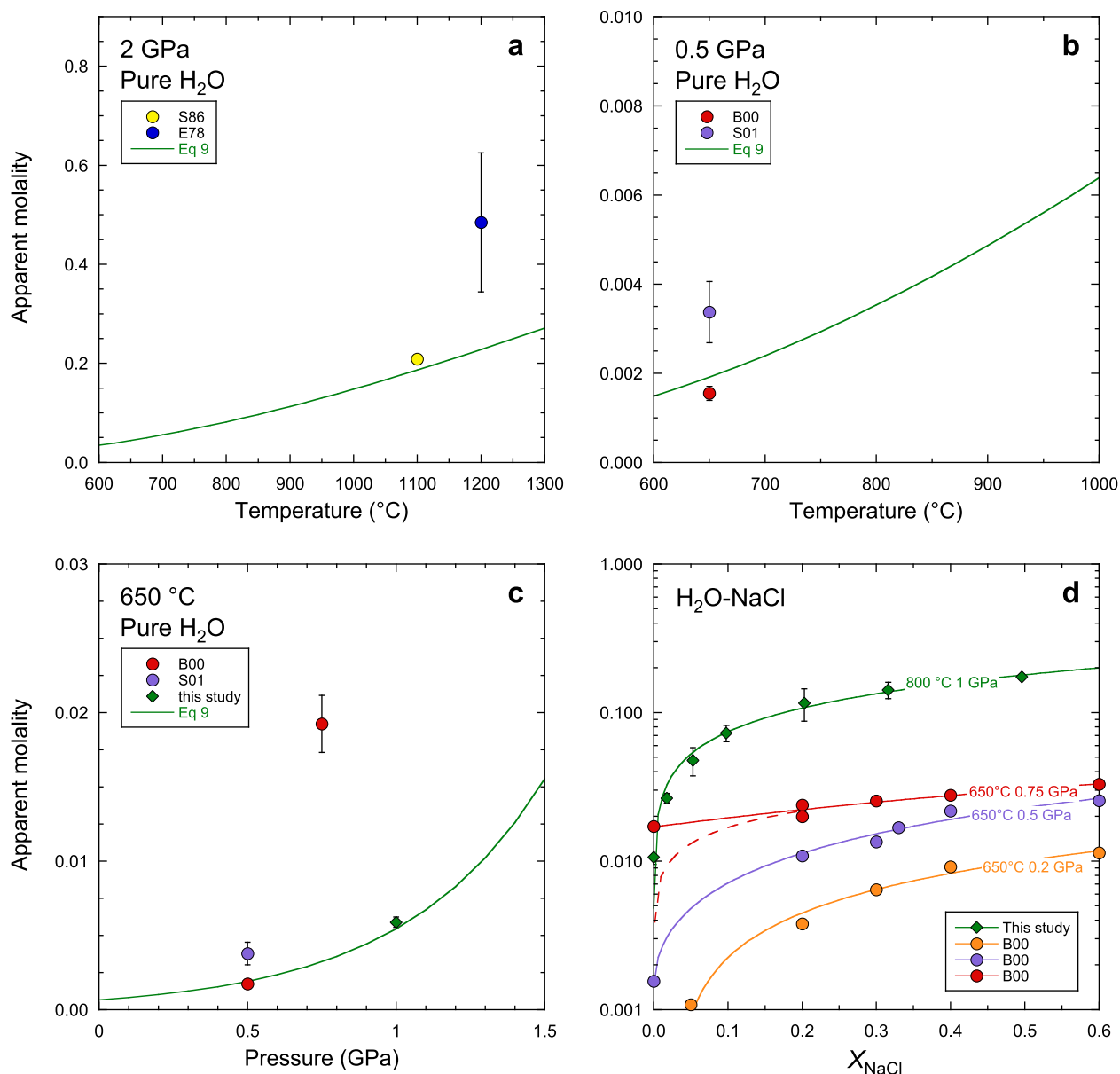
Fig. 9. Comparisons of diopside apparent solubility determined in this study (Eqs. (9) and (10), green curves) with results of previous work. (a) 2.0 GPa, pure H_2O (Schneider and Eggler, 1986 (S86); Eggler and Rosenhauer, 1978 (E78), blue circle). There is good agreement between our predicted values and the datum of Schneider and Eggler (1986). Discrepancy with the results of Eggler and Rosenhauer (1978) is likely due to their short run times, phase equilibrium methods, and possibly nonobservation of incongruent dissolution (see text). (b) 0.5 GPa, pure H_2O (Budanov and Shmulovich, 2000 (B00), red circle; Shmulovich et al., 2001 (S01), purple circle). Our predicted solubility at 650 °C lies between the previous results. (c) 650 °C, pure H_2O (Budanov and Shmulovich, 2000 (B00), red circles; Shmulovich et al., 2001 (S01), purple circle). The results are in reasonable agreement with the exception of the 0.75 GPa datum of Budanov and Shmulovich (2000). (d) 650 °C, H_2O-NaCl solutions (Budanov and Shmulovich, 2000 (B00) at 0.2 GPa (orange circles), 0.5 GPa (purple circles), and 0.75 Gpa (red circles). The Budanov and Shmulovich (2000) data at 0.2 and 0.5 GPa display a dependence on X_{NaCl} that is similar to that in our study, but apparent solubilities are lower, consistent with the lower P and T. In contrast, the data at 0.75 GPa display a different X_{NaCl} dependence, likely due to inaccurately high measured solubility in pure H_2O. A similar functional form of the X_{NaCl} dependence is obtained if the data are refit using the pure H_2O value predicted from Eq. (9) (dashed red line; see text). Errors in previous work are 2σ where given, and shown only where larger than symbols. (For interpretation of the references to color in the figure legend, the reader is referred to the web version of this article.)

whereas Mg increases with NaCl content, Si declines (Fig. 4b). Mg/Si in the fluid rises steadily with NaCl, but m_{Mg} is significantly lower than m_{Si} (Fig. 4c). Therefore, Si molality can again be used to compare to congruently dis-

solving minerals. Fig. 10a shows that, like quartz, Si molality in equilibrium with enstatite declines with X_{NaCl}, though to a much smaller degree. The enstatite trend lies between the forsterite and quartz trends.

The molality scale is based on the H_2O component of the solvent, so it helps differentiate between the role of the water and the role of NaCl in controlling solubility behavior. Declines with X_{NaCl}, as seen for quartz and enstatite, suggest that solute hydration controls dissolution. In contrast, an increase with X_{NaCl}, as for forsterite, diopside and wollastonite, implies that formation and stability of Cl- and Na- complexes primarily dictate solubility in salt solutions.

In detail, both solute hydration and Na- and Cl- complexing control dissolution behavior to varying degrees. Insight into their relative contributions can be obtained using mass-based or mole-fraction based solute concentra-

tions in the H_2O-NaCl solution (Fig. 10b and c). Concentrations in parts per million (ppm) for diopside and enstatite were computed using the sums of calculated solute masses. On this concentration scale (Fig. 10b), quartz and enstatite solubility decline in log-linear fashion. Forsterite, diopside and wollastonite increase sharply at low X_{NaCl}, then define weak maxima near $X_{NaCl} \sim 0.3$.

Concentrations on the mole-fraction scale (Fig. 10c) take explicit account of the dissociation of NaCl in the solution via

$$X_i = \frac{m_i}{m_i + 55.51 \left(\frac{1+(1+\alpha)X_{NaCl}}{X_{H_2O}} \right)} \tag{11}$$

(Newton and Manning, 2006), where α is the NaCl dissociation parameter calculated following Aranovich and Newton (1996), X_{NaCl} and X_{H2O} are calculated from bulk water and salt added to an experiment, and 55.51 is the number of moles in 1 kg H_2O. For congruently dissolving minerals, X_i is determined from the molality of i in solution. For diopside and enstatite, which dissolve incongruently, we calculate X_i using the sum of solute molalities. To highlight trends of solubility enhancement or suppression, mole fractions relative to those in pure H_2O are depicted. Fig. 10c clearly differentiates minerals for which NaCl suppresses solubility relative to pure H_2O (enstatite and quartz) from those for which it enhances solubility (forsterite, diopside, wollastonite). Of note is the much stronger relative enrichment of forsterite compared to diopside and wollastonite, which display analogous enhancement behavior.

The trends in Fig. 10c give insight into solute-solvent interactions that control solubility. The log-linear salting out of quartz in NaCl solutions is less pronounced than in CO_2 solutions at equal activities of H_2O (Newton and Manning, 2000a, 2009). This is likely a consequence of Na-Si complexing and/or NaCl-SiO_2 complexing (Newton and Manning, 2006, 2010, 2016). The smaller decline in enstatite solubility with X_{NaCl}, relative to quartz signals an important role for Mg-Cl complexing (as $MgCl^+$ or $MgCl_2$).
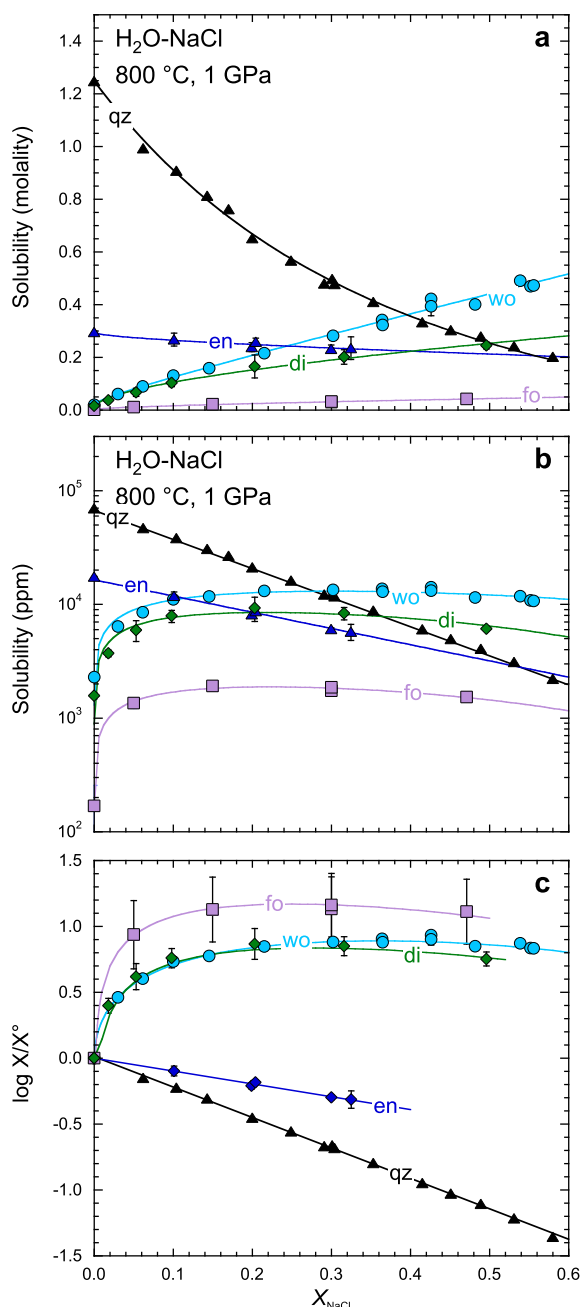
Fig. 10. Plots comparing the solubility behavior of selected minerals with increasing X_{NaCl} at 800 °C and 1 GPa, using different concentration scales. Minerals depicted are: quartz (black triangles), enstatite (dark blue triangles), forsterite (purple squares), wollastonite (light blue circles) and diopside apparent (dark green diamonds). (a) Mineral solubility on the molal concentration scale. Enstatite and diopside shown as Si molality, the most abundant solute. (b) Mineral solubility on parts per million concentration scale. Enstatite shown where coexisting with forsterite. (c) Mineral solubilities on mole fraction concentration scale (X), relative to the mole fraction in pure H_2O (X°). Enstatite and diopside solubilities depicted using total moles of solute, as calculated where coexisting with forsterite. The contrasting trends of solubility change with NaCl reflect omission (a) vs. inclusion (b and c) of NaCl in the solvent. 2σ errors shown where larger than symbol size; the comparatively large errors in forsterite in (c) arise from the projection method used to obtain solubility in pure H_2O (X°, see text). (For interpretation of the references to color in the figure legend, the reader is referred to the web version of this article.)

In contrast to quartz and enstatite, the solubilities in NaCl solutions of forsterite, diopside and wollastonite show enhancement (salting in) relative to solubilities in pure H_2O (Fig. 10c). For forsterite at 800 °C, the solubility at 30 mol% NaCl is about 15 times that in pure H_2O (at 900 °C, it is 30 times higher). Values of $\log X/X°$ rise to a maximum between X_{NaCl} of 0.2 to 0.3, then show a slight decline. The relative increase in diopside solubility is very similar to that observed for wollastonite. It was previously shown that wollastonite solubility displayed a maximum enhancement of ~8x at X_{NaCl} of ~0.33 before declining to higher X_{NaCl} (Newton and Manning, 2006). We observe similar behavior for diopside, which shows a maximum enhancement of 7x observed at $X_{NaCl} = 0.31$.

Insight into the nature of the solvent interactions that cause salting in Mg silicates can be gained in a manner similar to that for wollastonite, for which Newton and Manning (2006) suggested that the weak maximum is due to the formation of Ca chloride and a Na-Si hydroxide complexes. This results in the overall decline in relative solubility enhancement at high X_{NaCl} owing to a decrease in H_2O activity. Controls on the relative solubility pattern of forsterite can be constrained by expressing the dissolution reaction as

$$Mg_2SiO_4 + yNaCl + zH_2O = n \text{ solute species} \quad (12)$$
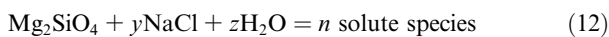
forsterite

Assuming ideal solution of solute species (Newton and Manning, 2006, 2010), the equilibrium constant K_{eq} for Equation (12) at a given P and T is

$$K_{eq} = \frac{X_{fo}^n}{a_{NaCl}^y a_{H_2O}^z} \quad (13)$$

where the a is the activity of the subscripted solvent component in their mixtures and X_{fo} is the mole fraction of Mg_2SiO_4 based on all molecules and ions of the solution. Assuming ideal mixing, the activities of NaCl and H_2O are, respectively,

$$a_{NaCl} = (1+\alpha)^{(1+\alpha)} \left(\frac{X_{NaCl}}{1+\alpha X_{NaCl}} \right)^{(1+\alpha)} \quad (14)$$
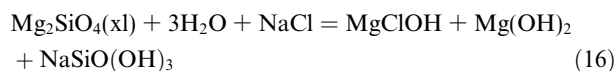
and

$$a_{H_2O} = \frac{X_{H_2O}}{1 + \alpha X_{H_2O}} \quad (15)$$

(Aranovich and Newton 1996), where α is again the measure of NaCl dissociation. This model yields $\alpha = 1.0$ at 800 °C, 1 GPa.
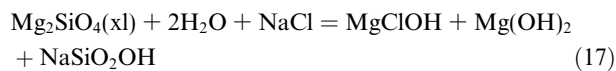
Assuming that y and z are integers and that X_{Fo} is too small to affect the activities in Eqs. (13) and (14), the forsterite solubility data may be fitted by least squares to determine y, z, n and K_{eq}. As an additional constraint, the relative solubility of a congruently dissolving mineral X_i is at a maximum with respect to X_{NaCl} when the latter quantity is equal to $y/(y + z)$ (Newton and Manning, 2010). This criterion limits the ratio y/z to between 0.3 and 0.5, based on the solubility measurements. Using the above equations, the optimal values of y, z and n were found to be 1, 3 and 3, respectively, at 800 °C, $K_{eq} = 8.9 \times 10^{-10}$, with a solubility

maximum at $X_{NaCl} = 0.25$. These results are shown with the purple line in Fig. 10c. At 900 °C a best fit is obtained with y, z and n of 1, 2 and 3, with a maximum at 0.33 and $K_{eq} = 4.3 \times 10^{-9}$ (not shown).

The number of discrete solute species per NaCl reacted is quite robust at $n = 3$. This suggests that Mg and Si dissolve independently, without Mg-silicate complexing, consistent with the conclusions drawn above. The Mg solute is likely to be a chloride, whereas the Si likely complexes with Na to produce a very soluble Na-silicate species. A number of combinations of species, charged and uncharged, may be imagined that satisfy reaction stoichiometry and charge balance. Suitable but non-unique reactions written as neutral solute species are:

$$Mg_2SiO_4(xl) + 3H_2O + NaCl = MgClOH + Mg(OH)_2$$
$$+ NaSiO(OH)_3 \quad (16)$$

at 800 °C, or

$$Mg_2SiO_4(xl) + 2H_2O + NaCl = MgClOH + Mg(OH)_2$$
$$+ NaSiO_2OH \quad (17)$$

at 900 °C. The higher hydration state of solutes at 800 °C than at 900 °C (H_2O/NaCl = 3:1 vs. 2:1) seems plausible in light of the expected effects of temperature.

The approach outlined above is strictly applicable only to congruently dissolving minerals. But it provides insights into solute species associated with the incongruent dissolution of diopside. Diopside solubility and solubility enhancement are very similar to wollastonite, which dissolves in H_2O-NaCl chiefly as very soluble Ca-chloride and hydrous Na-silicate complexes (Newton and Manning, 2006). In contrast, while the relative enhancement of forsterite solubility by NaCl is even greater than that of wollastonite and diopside (Fig. 10c), it is much lower on an absolute basis (Fig. 10a and b). The generally refractory nature of Mg relative to Ca at these conditions, which is expressed as solubilities and solubility enhancements that are lower for the Mg-bearing phases at all X_{NaCl}, suggests that Ca-chloride complexes are substantially more stable than Mg-chloride complexes at the experimental conditions.

4.4. Comparison to other minerals

Fig. 11 presents a compilation of solubility data at 800 °C and 1 GPa for many different mineral classes, including silicates, phosphates, sulfates, carbonates, oxides and halides. These data are presented in order of increasing solubility (in ppm) in pure H_2O (blue diamonds). Where available, solubilities at $X_{NaCl} \approx 0.1$ and $X_{NaCl} \approx 0.3$ are shown as red and green diamonds, respectively. While this comparison is restricted to experimentally studied minerals, several observations can still be made from the limited data set. First, solubilities of oxides of high field-strength elements in pure H_2O are lower than Ca-salts and silicates, consistent with the general expectation from ambient conditions that cations with high charge-to-radius ratio are relatively insoluble. In general, silicates have high solubility and Si-rich tectosilicates (quartz, albite) are more soluble in H_2O than neso- and inosilicates, consistent with the strong solubility

of silica and the SiO_2-rich nature of deep crustal fluids (Manning, 2018). With respect to changes due to NaCl addition, the enhancement in solubility of Ca-salts (phosphate, fluoride, sulfate, carbonate) continues to the highest NaCl concentrations, to X_{NaCl} at least 0.3, compared to that of corundum and silicates, for which there is either a plateau in enhancement or a decrease with salt addition. In addition, while all Ca-bearing minerals show solubility increases with NaCl, among the other oxides and silicates, only corundum and forsterite exhibit similar behavior, whereas quartz, enstatite and albite decrease in solubility with increasing X_{NaCl}.

While changes in solubility relative to that in pure H_2O are measures of the relative stabilities and hydration state of solute species (e.g., Newton and Manning, 2010), Fig. 11 suggests that roles for mineral constitution and structure can also be discerned. Fig. 12 compares solubilities in pure H_2O at 800 °C, 1 GPa, plotted versus cation radius, ionic potential and average force constant, a measure of bond strength (see spreadsheets 'Supplement Calculations 1' and 'Supplement Calculations 2' for values used in Fig. 12). Cation radii in Fig. 12a (Shannon, 1976) are shown as filled symbols when referring to the inter-radical cation in the mineral, and open symbols of the same color

when referring to the intra-radical cation(s) in the mineral structure. In the case of a mineral having more than one intra-radical cation, a weighted average of both cations are plotted according to mineral stoichiometry. For example, in grossular ($Ca_3Al_2Si_3O_{12}$) the inter-radical cation is Si^{4+}, with an effective ionic radius of 0.26 Å; and there are two intra-radical cations Ca^{2+} and Al^{3+}, with effective ionic radii of 1.12 and 0.535 Å, respectively. A value of 0.886 Å is plotted to represent the intra-radical cations, calculated using a weighted average based on mineral stoichiometry: $((1.12 \times 3) + (0.535 \times 2))/5 = 0.886$. In general, larger cations have weaker bonds, and we might expect that minerals with weaker bonds would be more soluble. However, comparing cation radii with mineral solubilities reveals no obvious solubility trends among minerals.

A plot of average ionic potential for each mineral (Fig. 12b), calculated according the equation z/r, where z is the charge of a cation, and r is its radius (again using effective ionic radii of Shannon, 1976), shows minerals clustering according to mineral class and the appearance of trends correlating mineral solubility and the ionic potentials of the mineral structures. Solubilities of fluorides, oxides and phosphates show a roughly linear negative correlation (on a log scale) with average ionic potential, while silicates
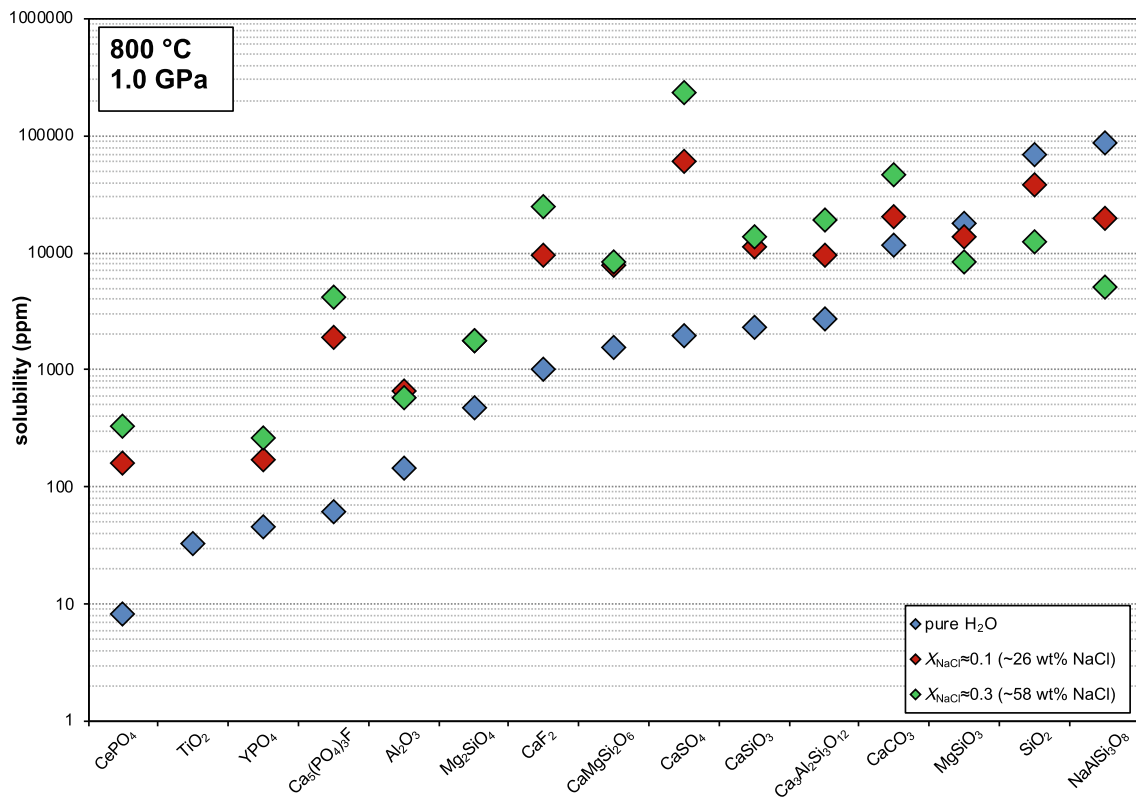

Fig. 11. Comparison of forsterite, enstatite and diopside solubilities from this study with other mineral solubility data from previous studies as a function of fluid NaCl content (X_{NaCl}) at 800 °C, 1.0 GPa. Solubilities here are presented in parts per million (ppm) on a log scale for more direct inter-mineral comparison. Minerals (x-axis) are ordered in terms of increasing solubility in pure H_2O. Forsterite solubility is low relative to other silicates such as quartz, wollastonite, grossular and diopside. Note the significant solubility enhancement experienced by Ca-salts (phosphate, fluoride, sulfate) in concentrated NaCl solutions, compared to that of silicates. Enstatite and quartz show the opposite behavior, with decreasing solubility in brines. Solubility data are from Newton and Manning (2000a, 2002a,b, 2005, 2006, 2007), Tropper and Manning (2007), Antignano and Manning (2008a,b), Tropper et al. (2011), Makhluf et al. (2016) and this study.
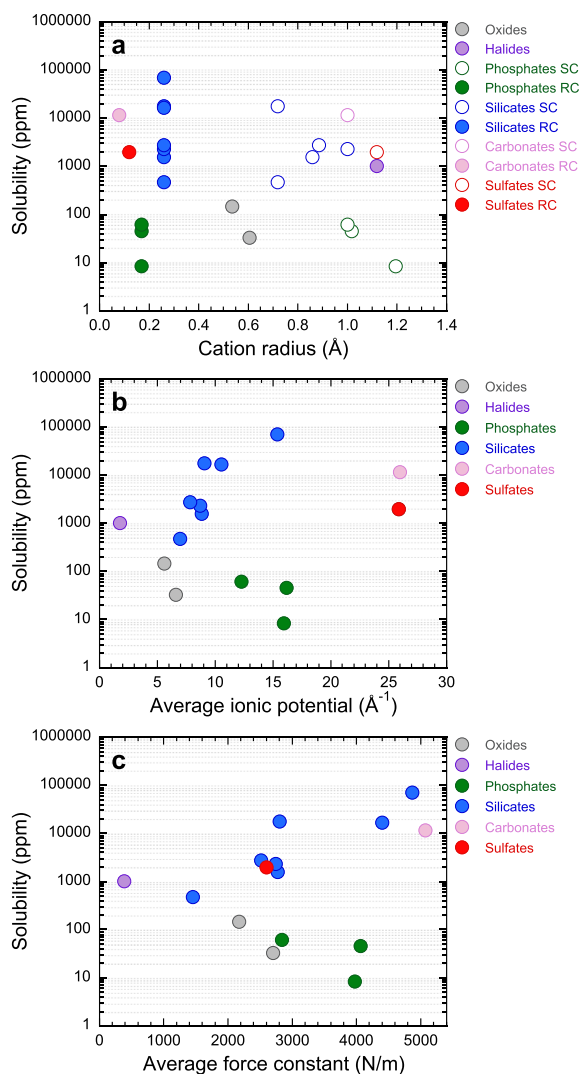
Fig. 12. Solubilities in ppm (log scale) of phosphate, oxide, silicate, halide, carbonate and sulfate minerals in pure H$_2$O at 800 °C and 1 GPa, plotted against (a) cation radius, (b) average ionic potential and (c) average force constant. The legend on the right applies generally to all plots, except in (a) filled symbols refer to the inter-radical cation in the mineral and open symbols of the same color refer to the intra-radical cation(s) in the mineral structure. In the case of a mineral having more than one intra-radical cation, a weighted average of both cations are plotted according to mineral stoichiometry. Average ionic potential in (b) is defined as cation charge (z) divided by radius (r) (cation radii used here are the effective ionic radii of Shannon (1976)). Average force constant (K_f) in (c) is a measure of bond strength calculated using Eq. (5) in Macris et al. (2015). See supplementary material for a complete explanation of the force constant calculations. Solubility data as in Fig. 11.

have a steeply positive correlation. The carbonate and sulfate minerals do not appear to lie on either trend. Ionic potentials are calculated for each cation in a mineral structure, then the average ionic potential is calculated using a weighted average of all cations according to mineral stoichiometry. Again using grossular as an example, the ionic potentials of Ca^{2+}, Al^{3+}, and Si^{4+} are 1.786, 5.607, and 15.38 Å^{-1}, respectively. The average ionic potential for

the mineral is calculated as the weighted average according to mineral stoichiometry:$((1.79 \times 3) + (5.61 \times 2) + (15.38 \times 3))/8 = 7.84$.

Another potential indicator of susceptibility to dissolution for a mineral is the strength of the bonds in the mineral's structure. The force constant (K_f) for a bond between cation i and anion j, is a measure of bond strength or stiffness, and is calculated according to the equation,

$$K_{f,ij} = \frac{z_i z_j e^2 (1-n)}{4\pi\varepsilon_o r_{ij}^3} \qquad (18)$$

where z_i and z_j are the cation and anion valences, ε_o is the dielectric constant (vacuum permittivity for simplicity), e is the charge of an electron, n is the exponent in the Born-Mayer formulation for ion repulsion (Born and Mayer, 1932), and r_{ij} is the equilibrium interionic distance between cation i and anion j (see Macris et al. (2015) and Young et al. (2009) for detailed discussions of this parameter and its applications). To calculate the average force constant for a mineral, we used the crystal structures program, CrystalMaker®, to determine the average bond lengths between each cation-anion bond pair in a mineral's structure, which were used as the equilibrium interionic distances, r_{ij}, in Eq. (18).

When plotting average force constant vs. mineral solubility (Fig. 12c), two clear trends emerge: (1) a negative (approximately) linear trend consisting of fluoride, oxide and phosphate minerals, which crosses (2) a positive, roughly linear trend consisting of silicate, carbonate and sulfate minerals. Trend (1) is consistent with the idea that, in comparatively simple structures, weaker bonds (lower average K_f) lead to higher solubilities in H$_2$O. Given the minerals that comprise trend (2), it may be that despite stronger average bonds in silicate, carbonate and sulfate minerals, the balance of solubility among constituents may supersede bond strength. For the silicate minerals, average force constant generally increases with SiO$_2$ content. The positively correlated rise in solubility may be related to the stability of silica in pure water. Similarly, the carbonate and sulfate anion groups in calcite and anhydrite likely have greater relative stability as aqueous solutes than fluoride and phosphate. However, these minerals are alone in their class (i.e., calcite is the only carbonate, and anhydrite is the only sulfate plotted), so more data is necessary to fully interpret their behavior in this context.

4.5. Geological applications

These experimental results allow evaluation of fluid composition along specific high P-T fluid flow paths in the lower crust and upper mantle, for model ultramafic rocks containing olivine, orthopyroxene (opx) and clinopyroxene (cpx). Regardless of setting, our results suggest that where fluids are relatively H$_2$O rich and NaCl poor, orthopyroxene solubility is substantially higher than olivine or clinopyroxene, so fluids will be rich in silica relative to Ca and Mg. The presence of cpx yields Ca > Mg. Hence, where all three phases are present, even in minor abundance, concentrations of major cations in associated fluids will scale as Si > Ca > Mg. In NaCl-rich fluids (brines),

cpx becomes the most soluble mineral, but the order of solute concentrations remains the same. Hence, $Si > Ca > Mg$ across the entire range of H_2O-NaCl concentrations at conditions investigated thus far.

In subduction zones, fluid moving towards the Earth's surface from the slab to the mantle wedge heats up as it decompresses. Temperature increase and pressure decrease have competing effects on mineral solubility in this system (e.g., Fig. 6 and Newton and Manning, 2002a). The spatial scales are such that, in the mantle wedge, temperature may increase greatly over a narrow depth range (e.g., Fig. 1a and Syracuse et al., 2010). Thus, we can predict that as a fluid moves from slab to wedge and therefore decompresses and heats up, forsterite, enstatite and diopside solubilities will all increase despite decreasing pressure. Fluids equilibrated with model ultramafic rocks containing olivine, opx and cpx along this path will increase in total dissolved solids at a given X_{NaCl}, with $Si > Ca > Mg$. This is consistent with theoretical predictions on the composition of fluids in equilibrium with eclogites (Manning, 1998), experimental investigations on fluid compositions in equilibrium with high-pressure mantle rocks (e.g., Schneider and Eggler, 1986; Ayers et al., 1997), and also manifested in vein minerals in blueschists and eclogites which are Na-Ca-Al-Si rich (Becker et al., 1999; Gao and Klemd, 2001) and poor in Mg. In lower-crustal settings, fluid flow paths can be expected to mainly involve cooling and decompression, resulting in declining solubilities while the solubility order is maintained. This can yield metasomatic addition of Si, Ca and Mg downstream through precipitation of CMSH minerals in flow conduits.

Our results have particular significance for Ca mobility in fluids interacting with ultramafic and mafic rocks. At all X_{NaCl} investigated, the solubility of wollastonite is greater than diopside, which in turn is greater than forsterite. As X_{NaCl} increases, these solubility differences are amplified. Brines in contact with ultramafic and mafic rocks at high pressures and temperatures will preferentially strip Ca relative to Mg, resulting in a Ca/Mg ratio of >1 in solution. These results provide a foundation for quantifying the nature of interaction between ultramafic rocks and complex brines in the deep crust and upper mantle.

In general, the high solubility of Ca minerals (silicates, carbonates, sulfates, phosphates; Fig. 11) in alkali halide-bearing solutions may have an important effect on processes affecting the upper mantle source regions for basaltic magmas. For example, O'Reilly and Griffin (2013) found evidence in mantle xenoliths for refertilization of depleted harzburgite by metasomatic introduction of Ca, Al and trace elements. They suggested that both carbonatitic and ultrasaline fluids could have accomplished the alteration. Newton and Manning (2002b) showed that calcite is so soluble in concentrated NaCl solutions at high temperatures and pressures that supercritical mixing occurs over a large portion of the system $CaCO_3$-H_2O-NaCl. In this regard, there may be a continuum of compositions between carbonate-rich and chloride-rich fluids capable of restoring fertility to depleted harzburgite. Evidence supporting the existence of such fluids include carbonatite samples retrieved from deep drill holes well below the circulation

of groundwater, which contain abundant halite intergrown with silicate minerals and carbonates (Kamenetsky et al., 2015), and the spectrum of fluid compositions found in diamonds grown in the presence of a fluid phase (Weiss et al., 2014, 2015).

Our results also provide insights into metasomatic processes at shallower crustal levels, as the element solubility order and role of NaCl are likely to be little affected by pressure. An example is the dunite and pyroxenite bodies found in the ultramafic sequences of some large layered intrusions, where monomineralic lenses, often discordant to the igneous layering, have received much discussion because some host deposits of the Pt-Group elements Pt, Ir, Os and Pd in associated chromitite lenses (e.g., in the Bushveld and Stillwater Complexes). Ophiolitic podiform chromitites are typically located within dunite lenses (Arai, 1997). There are diverse interpretations of the origins of dunite and pyroxenite veins in ultramafic bodies by magmatic processes (Kelemen et al., 1992; Tait and Jaupart, 1992; Batanova and Sobolev, 2000; Büchl et al., 2002; Scoon and Mitchell, 2004; Abbou-Kebir et al., 2011). An alternative is alteration by late-igneous or post-consolidation Cl-rich hydrothermal fluids (Schiffries, 1982; Schiffries and Rye, 1990). Balhaus and Stümpfl (1986) found halite-saturated brine inclusions in quartz from the highly mineralized Merensky Reef zone of the Bushveld, and Boudreau et al. (1986) found Cl enrichment of minerals in zones of the Stillwater complex. Our results, combined with those of Newton and Manning (2002a), lend support to this model in two ways. The first is the great pressure and temperature dependence of enstatite and diopside solubility. In the crustal pressure range up to 1.0 GPa the solubility of enstatite in pure H_2O increases by a factor of fifty between 0.2 GPa at 700 °C and 1.0 GPa at 900 °C (Newton and Manning 2002a). Diopside solubility behaves similarly, though changes with P and T are smaller. Pyroxenite veins are thus explainable by rising and cooling hydrothermal solutions. Second, our finding of great solubility increase of forsterite and diopside in NaCl-rich solutions could account for metasomatism at deep levels of a cooling gabbro/ultramafic intrusion, with deposition of dunite or clinopyroxenite veins, while the high solubility of enstatite in such fluids could cause desilication of harzburgite to dunite. Cl metasomatism and metal transport would be natural associates of brine percolation.

Finally, peridot gems of the Zabargad Island (Red Sea) peridotite contain inclusions of halite and fluid that indicate great crystal growth of forsterite in extremely concentrated brines (Clochiatti et al., 1981). The possible source of NaCl in this case is infiltration of sea water into hot, shallow peridotite. This occurrence shows that concentrated NaCl solutions retain great fluxing power for ferromagnesian silicates even at near-surface pressures.

5. CONCLUSIONS

1. Forsterite dissolution in H_2O-NaCl solutions was measured at 1 GPa, 800 °C and 900 °C. In pure H_2O at 800 °C, dissolution is very slightly incongruent, with

minute brucite flakes on the surface. Addition of excess silica allowed projection to obtain apparent solubility. At all other conditions forsterite dissolved congruently. Solubility isotherms show initial enhancement by addition of NaCl at both temperatures. The curves reach weak maxima at $X_{NaCl} \sim 0.25–0.33$. Mg-chloride and hydrous Na-silicate are likely the most abundant species in these solutions.

2. Enstatite dissolution in H_2O-NaCl solutions was measured at 1 GPa, 800 °C and 900 °C. Dissolution is incongruent, to forsterite + solutes, at all conditions studied. Additional experiments with excess SiO_2 reveal that only minor additional silica is required to suppress forsterite growth. Combination of the forsterite results permitted derivation of the compositions of fluids coexisting with enstatite + forsterite to constrain Si and Mg. Si and bulk solute concentrations decline slightly with rising NaCl; Mg content increases, similar to forsterite. Enstatite salts out with increasing NaCl. The behavior is similar to that of quartz, though the magnitude is less pronounced. This is likely because formation of Mg-chloride complexes promotes greater relative amounts of enstatite dissolution, leading to higher relative Si concentrations than in Mg-free, quartz-saturated solutions.

3. Diopside dissolution was investigated in pure H_2O at 0.7–1.5 GPa at 800 °C and at 650–900 °C at 1 GPa. Diopside solubility was also measured in H_2O-NaCl at 1 GPa and 800 °C. Diopside dissolves incongruently to forsterite + solutes at all conditions. In pure H_2O, apparent solubility rises with increasing temperature and pressure. Apparent solubility also rises with NaCl. Our new results are generally consistent with previous work. The compositions of H_2O-NaCl fluids could be derived at 800 °C, 1 GPa, where forsterite solubility was also determined. Results show that $m_{Si} > m_{Ca} > m_{Mg}$. The pattern of bulk diopside solubility enhancement is similar to that of wollastonite, and points to greater stability of Ca-chloride complexes relative to Mg-chloride complexes.

4. As a fluid moves from slab to wedge and therefore decompresses and heats up, forsterite, enstatite and diopside solubilities will all increase despite decreasing pressure. Fluids equilibrated with ultramafic rocks containing olivine, opx and cpx along this path will increase in total dissolved solids at a given X_{NaCl}, with Si > Ca > Mg. These fluids may then interact with lower mantle/upper crustal minerals assemblages and melts as they migrate, providing a mechanism for refertilization of depleted harzburgite.

5. In lower-crustal settings, fluid flow paths can be expected to mainly involve cooling and decompression, resulting in declining solubilities of forsterite, diopside and enstatite, while the solubility order is maintained. This can yield metasomatic addition of Si, Ca and Mg downstream through precipitation of CMSH minerals in flow conduits. Pyroxenite veins are thus explainable by rising and cooling hydrothermal solutions.

6. The significant solubility increase of forsterite and diopside in NaCl-rich solutions could account for metasomatism at deep levels of a cooling gabbro/ultramafic intrusion, with deposition of dunite or clinopyroxenite veins, while the high solubility of enstatite in such fluids could cause desilication of harzburgite to dunite.

Declaration of Competing Interest

The authors declare that they have no known competing financial interests or personal relationships that could have appeared to influence the work reported in this paper.

APPENDIX A. SUPPLEMENTARY MATERIAL

Supplementary data to this article can be found online at https://doi.org/10.1016/j.gca.2020.03.035.

REFERENCES

Abbou-Kebir K., Arai S. and Ceuleneer G. (2011) Origin of spinel-free dunite veins from northern Oman ophiolites: possible involvement of komatiitic melt. *J. Miner. Petrol. Sci.* **105**, 325–345.

Anderson T., O'Reilly S. Y. and Griffin W. L. (1984) The trapped fluid phase in upper mantle xenoliths from Victoria, Australia: implications for mantle metasomatism. *Contrib. Mineral. Petr.* **88**, 72–85.

Antignano A. and Manning C. E. (2008a) Fluorapatite solubility in H_2O and H_2O-NaCl at 700 to 900°C and 0.7 to 2.0 GPa. *Chem. Geol.* **251**, 112–119.

Antignano A. and Manning C. E. (2008b) Rutile solubility in H_2O, H_2O-SiO_2, and H_2O-$NaAlSi3O_8$ fluids at 0.7-2.0 GPa and 700–1000 °C: implications for mobility of nominally insoluble elements. *Chem. Geol.* **255**, 283–293.

Arai S. (1997) Control of wall-rock compositions on the formation of podiform chromitites as a result of magma-peridotite interaction. *Resour. Geol.* **47**, 177–187.

Aranovich L. Y. and Newton R. C. (1996) H_2O activity in concentrated NaCl solutions at high pressures and temperatures measured by the brucite-periclase equilibrium. *Contrib. Mineral. Petr.* **125**, 200–212.

Ayers J., Dittmer S. K. and Layne G. D. (1997) Partitioning of elements between peridotite and H_2O at 2.0-3.0 GPa and 900–110°C, and application to models of subduction zone processes. *Earth Planet. Sc. Lett.* **150**, 381–398.

Balhaus C. G. and Stümpfl E. F. (1986) Sulfide and platinum mineralization in the Merensky Reef: evidence from hydrous silicates and fluid inclusions. *Contrib. Mineral. Petr.* **94**, 193–204.

Barnes J. D., Manning C. E., Scambelluri M. and Selverstone J. (2018) The behavior of halogens during subduction-zone processes. In *The Role of Halogens in Terrestrial and Extraterrestrial Geochemical Processes* (eds. D. E. Harlov and L. Aranovich). Springer Geochemistry, pp. 545–590.

Batanova V. G. and Sobolev A. V. (2000) Compositional hetero-geneity in subduction-related mantle peridotite, Troodos Massif, Cyprus. *Geology* **28**, 55–58.

Becker H., Jockum K. P. and Carlson R. W. (1999) Constraints from high-pressure veins in eclogites on the composition of hydrous fluids in subduction zones. *Chem. Geol.* **160**, 291–308.

Born M. and Mayer J. E. (1932) Lattice theory of ionic crystals. *Z. Phys* **75**, 1–18.

Boudreau A. C., Mathez E. A. and McCallum I. S. (1986) Halogen geochemistry of the Stillwater and Bushveld Complexes: evidence for transport of the platinum group elements by Cl-rich fluids. *J. Petrol.* **27**, 967–986.

Büchl A., Brügmann G., Batanova G., Münker C. and Hofmann A. W. (2002) Melt percolation monitored by Os isotopes and HSE abundances: a case study from the mantle section of the Troodos Ophiolite. *Earth Planet. Sc. Lett.* **204**, 385–402.

Budanov S. V. and Shmulovich K. I. (2000) Experimental determination of diopside solubility in H_2O-NaCl fluids at 650 °C and pressures of 2–7.5 kbar. *Geochem. Int+.* **38**, S237–S243.

Clochiatti R., Messare O. and Jehanno C. (1981) Origine hydrothermal des olivines gemmes de l'ile de Zabargad (St. John), Mer Rouge, par l'étude de leurs inclusions. *Bulletin Minéralogique* **104**, 354–360.

Connolly J. A. D. (2005) Computation of phase equilibria by linear programming: a tool for geodynamic modeling and its application to subduction zone decarbonation. *Earth Planet. Sci. Lett.* **236**, 524–541.

Connolly J. and Kerrick D. (1987) An algorithm and computer program for calculating composition phase diagrams. *Calphad* **11**, 1–55.

Davis F. A., Tangeman J. A., Tenner T. J. and Hirschmann M. M. (2009) The composition of KLB-1 peridotite. *Am. Mineral.* **94**, 176–180.

Eggler D. H. and Rosenhauer M. (1978) Carbon dioxide in silicate melts; II, solubilities of CO_2 and H_2O in $CaMgSi_2O_6$ (diopside) liquids and vapors at pressures to 40 kb. *Am. J. Sci.* **278**, 64–94.

Frantz J. D. and Popp R. K. (1979) Mineral-solution equilibria—I. An experimental study of complexing and thermodynamic properties of aqueous $MgCl_2$ in the system $MgO-SiO_2-H_2O$-HCl. *Geochim. Cosmochim. Acta* **43**, 1223–1239.

Gao J. and Klemd R. (2001) Primary fluids entrapped at blueschist to eclogite transition: evidence from the Tianshan meta-subduction complex in northwestern China. *Contrib. Mineral. Petr.* **142**, 1–14.

Green E. C. R., White R. W., Diener J. F. A., Powell R., Holland T. J. B. and Palin R. M. (2016) Activity–composition relations for the calculation of partial melting equilibria in metabasic rocks. *J. Metamorph. Geol.* **34**, 845–869.

Hemley J. J., Montoya J. W., Christ C. L. and Hostetler P. B. (1977a) Mineral equilibria in the $MgO-SiO_2-H_2O$ system; I, Talc-chrysotile-forsterite-brucite stability relations. *Am. J. Sci.* **277**, 322–351.

Hemley J. J., Montoya J. W., Shaw D. R. and Luce R. W. (1977b) Mineral equilibria in the $MgO-SiO_2-H_2O$ system; II, Talc-antigorite-forsterite-anthophyllite-enstatite stability relations and some geologic implications in the system. *Am. J. Sci.* **277**, 353–383.

Holland T. J. B. and Powell R. (1998) An internally consistent thermodynamic data set for phases of petrological interest. *J. Metamorph. Geol.* **16**, 309–343.

Holland T. J. B., Hudson N. F., Powell R. and Harte B. (2013) New thermodynamic models and calculated phase equilibria in NCFMAS for basic and ultrabasic compositions through the transition zone into the uppermost lower mantle. *J. Petrol.* **54**, 1901–1920.

Holland T. J. B. and Powell R. (2011) An improved and extended internally consistent thermodynamic dataset for phases of petrological interest, involving a new equation of state for solids. *J. Metamorph. Geol.* **29**, 333–383.

Huang F. and Sverjensky D. A. (2019) Extended deep earth water model for predicting major element mantle metasomatism. *Geochim. Cosmochim. Acta* **254**, 192–230.

Ito J. (1975) High temperature solvent growth of orthoenstatite, $MgSiO_3$, in air. *Geophys. Res. Lett.* **2**, 533–536.

Jennings E. S. and Holland T. J. B. (2015) A simple thermodynamic model for melting of peridotite in the system NCFMA-SOCr. *J. Petrol.* **56**, 869–892.

Kamenetsky V. S., Mitchell R. H., Maas R., Giuliani A., Gaboury D. and Zhitova L. (2015) Chlorine in mantle-derived carbonatite melts revealed by halite in the St.-Honoré intrusion (Québec, Canada). *Geology* **43**, 687–690.

Kawamoto T., Matsukage K. N., Mibe K., Isshiki M., Nishimura K., Ishimatsu N. and Ono S. (2004) Mg/Si ratios of aqueous fluids coexisting with forsterite and enstatite based on the phase relations in the $Mg_2SiO_4-SiO_2-H_2O$ system. *Am. Mineral.* **89**, 1433–1437.

Kawamoto T., Yoshikawa M., Kumagai Y., Mirabueno M. H. T., Okuno M. and Kobayashi T. (2013) Mantle wedge infiltrated with saline fluids from dehydration and decarbonation of subducting slab. *P. Natl. Acad. Sci.* **110**, 9663–9668.

Kelemen P. B., Dick H. J. and Quick J. E. (1992) Formation of harzburgite by pervasive melt/rock reaction in the upper mantle. *Nature* **358**, 635–641.

Keppler H. (2017) Fluids and trace element transport in subduction zones. *Am. Mineral.* **102**, 5–20.

Luce R. W., Cygan G. L., Hemley J. J. and D'Angelo W. M. (1985) Some mineral stability relations in the system $CaO-MgO-SiO_2-H_2O$-HCl. *Geochim. Cosmochim. Acta* **49**, 525–538.

Macris C. A., Manning C. E. and Young E. D. (2015) Crystal chemical constraints on inter-mineral Fe isotope fractionation and implications for Fe isotope disequilibrium in San carlos mantle xenoliths. In *Geochim. Cosmochim. Acta*, 154, pp. 168–185. Geochim. Cosmochim. Acta.

Makhluf A. R., Newton R. C. and Manning C. E. (2016) Hydrous albite magmas at lower crustal pressure: new results on liquidus H_2O content, solubility, and H_2O activities at 1.0 GPa. *Contrib. Mineral. Petr.* **171**, 75–93.

Manning C. E. (1994) The solubility of quartz in H_2O in the lower crust and upper mantle. *Geochim. Cosmochim. Acta* **58**, 4831–4839.

Manning C. E. (1998) Fluid composition at the blueschist-eclogite transition in the model system $Na_2O-MgO-Al_2O_3-SiO_2-H_2O$-HCl. *Schweiz. Mineral. Petrogr. Mitt.* **78**, 225–242.

Manning C. E. (2018) Fluids of the lower crust: deep is different. *Annu. Rev. Earth Planet. Sci.* **46**, 67–97.

Manning C. E. and Aranovich L. Y. (2014) Brines at high pressure and temperature: thermodynamic, petrologic and geochemical effects. *Precambrian Res.* **253**, 6–16.

Manning C. E. and Boettcher S. L. (1994) Rapid-quench hydrothermal experiments at mantle pressures and temperatures. *Am. Mineral.* **79**, 1153–1158.

Métrich N. and Wallace P. J. (2008) Volatile abundances in basaltic magmas and their degassing paths tracked by melt inclusions. *Rev. Mineral. Geochem.* **69**, 363–402.

Mibe K., Fujii T. and Yasuda A. (2002) Composition of aqueous fluid coexisting with mantle minerals at high pressure and its bearing on the differentiation of Earth's mantle. *Geochim. Cosmochim. Acta* **66**, 2273–2285.

Nakamura Y. and Kushiro I. (1974) Composition of the gas phase in $Mg_2SiO_4-SiO_2-H_2O$ at 15 kbar. *Carnegie I. Wash.* **73**, 255–258.

Newton R. C. and Manning C. E. (2000a) Quartz solubility in H$_2$O-NaCl and H$_2$O-CO$_2$ solutions at deep crust-upper mantle pressures and temperatures: 2–15 kbar and 500–900 °C. *Geochim. Cosmochim. Acta* **64**, 2993–3005.

Newton R. C. and Manning C. E. (2000b) Metasomatic phase relations in the system CaO-MgO-SiO$_2$-H$_2$O-NaCl at high temperatures and pressures. *Int. Geol. Rev.* **42**, 152–162.

Newton R. C. and Manning C. E. (2002a) Solubility of enstatite + forsterite in H$_2$O at deep crust/upper mantle conditions: 4 to 15 kbar and 700 to 900 °C. *Geochim. Cosmochim. Acta* **66**, 4165–4176.

Newton R. C. and Manning C. E. (2002b) Experimental determination of calcite solubility in H$_2$O-NaCl solutions at deep crust/upper mantle pressures and temperatures: implications for metasomatic processes in shear zones. *Am. Mineral.* **87**, 1401–1409.

Newton R. C. and Manning C. E. (2005) Solubility of anhydrite, CaSO$_4$, in NaCl-H$_2$O solutions at high pressures and temperatures: applications to fluid-rock interaction. *J. Petrol.* **46**, 701–716.

Newton R. C. and Manning C. E. (2006) Solubilities of corundum, wollastonite and quartz in H$_2$O-NaCl solutions at 800 °C and 10 kbar: interaction of simple minerals with brines at high pressure and temperature. *Geochim. Cosmochim. Acta* **70**, 5571–5582.

Newton R. C. and Manning C. E. (2007) Solubility of grossular, Ca$_3$Al$_2$Si$_3$O$_{12}$, in H$_2$O-NaCl solutions at 800°C and 10 kbar, and the stability of garnet in the system CaSiO$_3$-Al$_2$O$_3$- H$_2$O-NaCl. *Geochim. Cosmochim. Acta* **71**, 5191–5202.

Newton R. C. and Manning C. E. (2009) Hydration state and activity of aqueous silica in H$_2$O-CO$_2$ fluids at high pressure and temperature. *Am. Mineral.* **94**, 1287–1290.

Newton R. C. and Manning C. E. (2010) Role of saline fluids in deep-crustal and upper-mantle metasomatism: insights from experimental studies. *Geofluids* **10**, 58–72.

Newton R. C. and Manning C. E. (2016) Evidence for SiO$_2$-NaCl complexing in H$_2$O-NaCl solutions at high pressure and temperature. *Geofluids* **16**, 342–348.

Newton R. C., Aranovich L. Y., Hansen E. C. and Vandenheuvel B. A. (1998) Hypersaline fluids in Precambrian deep-crustal metamorphism. *Precambrian Res.* **91**, 41–63.

O'Reilly S. Y. and Griffin W. L. (2013) Mantle metasomatism. In *Metasomatism and Chemical Transformation of Rock* (eds. D. E. Harlov and H. Austrheim). Springer, pp. 471–533.

Padrón-Navarta J. A., Sánchez-Vizcaíno V. L., Hermann J., Connolly J. A. D., Garrido C. J., Gómez-Pugnaire M. T. and Marchesi C. (2013) Tschermak's substitution in antigorite and consequences for phase relations and water liberation in high-grade serpentinites. *Lithos* **178**, 186–196.

Philippot P. and Selverstone J. (1991) Trace-element-rich brines in eclogitic veins: implications for fluid composition and transport during subduction. *Contrib. Mineral. Petr.* **106**, 417–430.

Ryabchikov I. D., Schreyer W. and Abraham K. (1982) Compositions of aqueous fluids in equilibrium with pyroxenes and olivines at mantle pressures and temperatures. *Contrib. Mineral. Petr.* **79**, 80–84.

Scambelluri M. and Philippot P. (2001) Deep fluids in subduction zones. *Lithos* **55**, 213–227.

Schiffries C. M. (1982) The petrogenesis of a platiniferous dunite pipe in the Bushveld Complex: infiltration metasomatism by a chloride solution. *Econ. Geol.* **77**, 1439–1453.

Schiffries C. M. and Rye D. M. (1990) Stable isotope systematics of the Bushveld Complex: II. Constraints on hydrothermal processes in layered intrusions. *Am. J. Sci.* **290**, 209–245.

Schneider M. E. and Eggler D. H. (1986) Fluids in equilibrium with peridotite minerals: implications for mantle metasomatism. *Geochim. Cosmochim. Acta* **50**, 711–724.

Scoon R. M. and Mitchell A. A. (2004) Petrogenesis of discordant magnesian dunite pipes from the central sector of the eastern Bushveld complex with emphasis on the Winaarshoek Pipe and disruption of the Merensky Reef. *Econ. Geol.* **99**, 517–541.

Shannon R. D. (1976) Revised effective ionic radii and systematic studies of interatomic distances in halides and chalcogenides. *Acta Crystallogr. Sect. A: Cryst. Phys. Diffract. Theoret. Gen. Crystallogr.* **32**, 751–767.

Shmelev V. R. (2011) Mantle ultrasbasites of ophiolite complexes in the Polar Urals: Petrogenesis and geodynamic consequences. *Petrology* **19**, 618–640.

Shmulovich K., Graham C. and Yardley B. (2001) Quartz, albite and diopside solubilities in H$_2$O-NaCl and H$_2$O-CO$_2$ fluids at 0.5-0.9 GPa. *Contrib. Mineral. Petr.* **141**, 95–108.

Shmulovich K. I., Yardley B. W. D. and Graham C. M. (2006) Solubility of quartz in crustal fluids: experiments and general equations for salt solutions and H$_2$O–CO$_2$ mixtures at 400–800°C and 0.1–0.9 GPa. *Geofluids* **6**, 154–167.

Stalder R., Ulmer P., Thompson A. B. and Gunther D. (2001) High pressure fluids in the system MgO-SiO$_2$-H$_2$O under upper mantle conditions. *Contrib. Mineral. Petr.* **140**, 607–618.

Sverjensky D. A., Shock E. L. and Helgeson H. C. (1997) Prediction of the thermodynamic properties of aqueous metal complexes to 1000 C and 5 kb. *Geochim. Cosmochim. Acta* **61**, 1359–1412.

Sverjensky D. A., Harrison B. and Azzolini D. (2014) Water in the deep Earth: the dielectric constant and the solubilities of quartz and corundum to 60 kb and 1200 C. *Geochim. Cosmochim. Acta* **129**, 125–145.

Syracuse E. M., van Keken P. E. and Abers G. A. (2010) The global range of subduction zone thermal models. *Phys. Earth Planet. Int.* **183**, 73–90.

Tait S. and Jaupart C. (1992) Compositional convection in a reactive crystalline mush and melt differentiation. *J. Geophys. Res.* **97**, 6735–6756.

Takei H. and Hosoya S. (1985) Growth of MnSiO$_3$ and (Mn, Mg) SiO$_3$ crystals by the floating-zone method. *J. Cryst. Growth* **71**, 17–22.

Till C. B., Grove T. L. and Withers A. C. (2012) The beginnings of hydrous mantle wedge melting. *Contrib. Mineral. Petrol.* **163**, 669–688.

Tiraboschi C., Tumiati S., Sverjensky D., Pettke T., Ulmer P. and Poli S. (2018) Experimental determination of magnesia and silica solubilities in graphite-saturated and redox-buffered high-pressure COH fluids in equilibrium with forsterite + enstatite and magnesite + enstatite. *Contrib. Mineral. Petrol.* **173**, 2.

Tropper P. and Manning C. E. (2007) The solubility of fluorite in H$_2$O and H$_2$O-NaCl at high pressure and temperature. *Chem. Geol.* **242**, 299–306.

Tropper P., Manning C. E. and Harlov D. (2011) Solubility of CePO$_4$ monazite and YPO$_4$ xenotime in H$_2$O and H$_2$O-NaCl at 800 °C and 1 GPa: implications for REE and Y transport during high-grade metamorphism. *Chem. Geol.* **282**, 58–66.

Wallace P. J. (2005) Volatiles in subduction zone magmas: concentrations and fluxes based on melt inclusion and volcanic gas data. *J. Volcanol. Geoth. Res.* **140**, 217–240.

Weiss Y., Kiflawi I., Davies N. and Navon O. (2014) High-density fluids and the growth of monocrystalline diamonds. *Geochim. Cosmochim. Acta* **141**, 145–159.

Weiss Y., McNeill J., Pearson D. G., Nowell G. M. and Ottley C. J. (2015) Highly saline fluids from a subducting slab as the source for fluid-rich diamonds. *Nature* **524**, 339–342.

White R. W., Powell R., Holland T. J. B., Johnson T. E. and Green E. C. R. (2014) New mineral activity-composition relations for thermodynamic calculations in metapelitic systems. *J. Metamorph. Geol.* **32**, 261–286.

Wolery T. J. (1992) EQ3NR, a computer program for geochemical aqueous speciation-solubility calculations: Theoretical manual, users guide, and related documentation (Version 7.0); Part 3 (No. UCRL-MA-110662-Pt. 3). Lawrence Livermore National Lab., CA (United States).

Wolery T. J. and Daveler S. A. (1992). EQ6, a computer program for reaction path modeling of aqueous geochemical systems: Theoretical manual, users guide, and related documentation (Version 7.0); Part 4 (No. UCRL-MA-110662-Pt. 4). Lawrence Livermore National Lab., CA (United States).

Wykes J. L., Newton R. C. and Manning C. E. (2008) Solubility of andradite, $Ca_3Fe_2Si_3O_{12}$, in a 10 mole % NaCl solution at 800° C and 10 kbar: implications for the metasomatic origin of grandite garnet in calc-silicate granulites. *Am. Mineral.* **93**, 886–892.

Yardley B. W. D. and Graham J. T. (2002) The origins of salinity in metamorphic fluids. *Geofluids* **2**, 249–256.

Yardley B. W. D. and Bodnar R. J. (2014) Fluids in the continental crust. *Geochem. Perspect.* **3**, 1–2.

Young E. D., Tonui E., Manning C. E., Schauble E. and Macris C. A. (2009) Spinel–olivine magnesium isotope thermometry in the mantle and implications for the Mg isotopic, composition of Earth. In *Earth Planet. Sci. Lett.*, 288, pp. 524–533. Earth Planet. Sci. Lett..

Zhang Y. G. and Frantz J. D. (2000) Enstatite-forsterite-water equilibria at elevated temperatures and pressures. *Am. Mineral.* **85**, 918–925.

Associate editor: Chen Zhu